Topological Tuning of DNA Mobility in Entangled Solutions of Supercoiled Plasmids

Jan Smrek[1], Jonathan Garamella[2],
Rae Robertson-Anderson[2], Davide Michieletto[3,4,*]

[1]Faculty of Physics, University of Vienna, Boltzmanngasse 5, A-1090 Vienna, Austria
[2]Department of Physics and Biophysics, University of San Diego
San Diego, CA 92110, USA
[3]School of Physics and Astronomy, University of Edinburgh
Peter Guthrie Tait Road, Edinburgh, EH9 3FD, UK
[4]MRC Human Genetics Unit, Institute of Genetics and Molecular Medicine
University of Edinburgh, Edinburgh EH4 2XU, UK
[*]To whom correspondence should be addressed; E-mail: davide.michieletto@ed.ac.uk

Ring polymers in dense solutions are among the most intriguing problems in polymer physics. Thanks to its natural occurrence in circular form, DNA has been extensively employed as a proxy to study the fundamental physics of ring polymers in different topological states. Yet, torsionally constrained – such as supercoiled – topologies have been largely neglected so far. The applicability of existing theoretical models to dense supercoiled DNA is thus unknown. Here we address this gap by coupling large-scale Molecular Dynamics simulations with Differential Dynamic Microscopy of entangled supercoiled DNA plasmids. We discover that, unexpectedly, larger supercoiling increases the size of entangled plasmids and concomitantly induces an enhancement in DNA mobility. These findings are reconciled as due to supercoiling-driven asym-

metric and double-folded plasmid conformations which reduce inter-plasmids entanglements and threadings. Our results suggest a way to topologically tune DNA mobility via supercoiling, thus enabling topological control over the (micro)rheology of DNA-based complex fluids.

Introduction

The deoxyribonucleic acid (DNA) is not only the central molecule of life but it is now increasingly employed for bio-compatible and responsive materials – such as DNA hydrogels (*1*) and origami (*2*) – with applications in medicine and nanotechnology (*3*). One feature that renders DNA a unique polymer is its ability to encode information, and this is now extensively leveraged to make complex structures (*3, 4*) and even self-replicating materials (*5*); another feature that distinguishes DNA from other synthetic polymers is its unique geometry, i.e. that of a (right-handed) helix with a well-defined pitch, which entails that DNA can display both bending and torsional stiffness (*6*). Unlike DNA's information-encoding capabilities, its geometrical features are far less exploited to create synthetic materials. In fact, DNA is at present largely employed to make up biopolymer complex fluids in its simplest geometrical forms, i.e. that of a linear or relaxed circular (torsionally unconstrained) molecule (*7–9*). In spite of this, most naturally occurring DNA is under torsional and topological constraints, either because it is circular and non-nicked, as in bacteria (*10*), or because of the binding of proteins that restrict the relative rotation of base-pairs, as in eukaryotes (*11–13*). The torsional stress stored in a closed DNA molecule cannot be mechanically relaxed (in absence of Topoisomerase proteins) but only re-arranged or converted into bending in order to minimise the overall conformational free energy (*14, 15*). This entails that supercoiling – the linking deficit between sister DNA strands with respect to their relaxed state – can carry conformational information (*16*) which can affect the static and dynamic properties of DNA plasmids (*14*) and even regulate gene tran-

scription (*17*). Here, we propose that supercoiling may also be leveraged to tune the dynamics of DNA plasmids in solution, thus potentially allowing for fine control over the rheology of DNA-based complex fluids in a way that is orthogonal to varying DNA length (*18*), concentration (*19*) or architecture (*7, 20*). Finally, entangled solutions of DNA plasmids are not only interesting due to their potential applications in bio and nanotechnology, but also as they enable us to study fundamental questions on the physics of ring polymers – one of the most active fields of soft matter research (*21–29*) – thanks to the extremely precise control over DNA lengths and topology (*7–9*) and access to sophisticated visualisation techniques (*30*).

To characterise the effect of DNA supercoiling on the rheology of entangled solutions of plasmids, here we perform large scale Molecular Dynamics simulations of entangled DNA plasmids (Fig. 1A-C), modelled as coarse-grained twistable chains (*31*). We discover that while isolated DNA plasmids typically display a collapse with increasing levels of supercoiling (estimated via simulations (*32*) or gel electrophoresis (*33*)), here we show that entangled DNA plasmids typically increase their average size with supercoiling. Importantly, we further discover that in spite of this swelling, larger supercoiling is accompanied by an *enhanced* mobility of the plasmids. This finding is counter-intuitive and in marked contrast with standard polymer systems (*34*) in which larger polymer sizes correlate with slower diffusion. This speed up is also observed in Differential Dynamic Microscopy experiments performed on entangled plasmids with different supercoiling degrees. Finally, we use sophisticated techniques involving minimal surface construction and primitive path analysis to quantify the abundance of threadings and entanglements between plasmids in solution and discover that larger supercoiling decreases both of these topological constraints, in turn explaining the enhanced mobility.

We argue that our results will be key to enabling the design of complex fluids with rheology that can be precisely tuned using a combination of DNA length, concentration, topology and supercoiling. Beyond providing blueprints for realising the next-generation of biomimetic

DNA-based materials, our results can also shed light into the dynamics of DNA *in vivo*.

Results

Computational Model for DNA plasmids

DNA is represented as a twistable elastic chain (*31*) made of beads of size $\sigma_b = 2.5$ nm $= 7.35$ bp connected by finitely-extensible springs and interacting via a purely repulsive Lennard-Jones potential to avoid spontaneous chain-crossing (*35*) (see Fig. 1). In addition to these potentials, a bending stiffness of $l_p = 50$ nm (*6*) is set via a Kratky-Porod term and two torsional springs (dihedrals) constrain the relative rotation of consecutive beads, ψ, at a user-defined value ψ_0. The torsional angle between consecutive beads ψ is determined by decorating each bead with three patches which provides a reference frame running along the DNA backbone. We finally impose a stiff harmonic spring to constrain the tilt angle $\theta = \pi$ so to align the frame with the backbone, i.e. along its local tangent (see Fig. 1D). The simulations are performed at fixed monomer density $\rho\sigma_b^3 = 0.08$ (corresponding to a volume fraction $\phi = 4\%$ and $\phi/\phi^* \simeq 16$ with $\phi^* = 0.26\%$) and by evolving the equation of motion for the beads coupled to a heat bath in LAMMPS (*36*) (see Methods).

The user-defined angle ψ_0 directly determines the thermodynamically preferred pitch of the twistable chains as $p = 2\pi/\psi_0$ and, in turn, this fixes the preferred linking number to $Lk = M/p$, where M is the number of beads in the plasmid. The twist is enforced by an harmonic potential with stiffness $\kappa_t = 50\sigma_b = 125$ nm comparable with the torsional persistence length of DNA (*6*). In this model, the degree of supercoiling is defined as $\sigma \equiv Lk/M = 1/p$. The twist is set by initialising the patchy-polymer as a flat ribbon and by subsequently slowly increasing the stiffness of the potential associated with the twist degree of freedom. Ultimately, by imposing the angle ψ_0 one can achieve the desired σ (which may be zero, if $\psi_0 = 0$ or $p = \infty$). It should be noted that we will also consider non-torsionally constrained plasmids in which the torsional

stiffness is set to $\kappa_t = 0$ mimicking nicked circular plasmids. We recall that for supercoiled circular DNA, the exchange of local torsion (twist Tw) into bending (writhe Wr) must obey the White-Fuller-Călugăreanu (WFC) (*37*) theorem, i.e. $Lk = Tw + Wr$, thus conserving the linking number Lk (and thus the supercoiling $\sigma = Lk/M$) between the two DNA single strands (Fig. 1B-D). Notice that our polymer model is symmetric with respect to supercoiling; we will thus refer to σ without specifying its sign. Finally, by simulating an ensemble of linear DNA molecules, we have computed the entanglement length for this model to be $M_{e,linear} = 54 \pm 2$ beads (about 400 bp) via standard primitive path analysis (see SI).

Supercoiling Increases the Average Size of DNA Plasmids in Entangled Conditions

The conformational properties of polymers in solution are typically studied in terms of the gyration tensor

$$R_T^{\alpha\beta} = \frac{1}{2M^2} \sum_{i,j=1}^{M} \left(r_i^\alpha - r_j^\alpha\right) \left(r_i^\beta - r_j^\beta\right) \tag{1}$$

where r_i^α denotes the coordinate α of the position of bead i. The (square) radius of gyration is then defined as the trace, $R_g^2 \equiv \mathrm{Tr}[\mathrm{R_T}]$. Interestingly, we find that the time and ensemble average of R_g^2 scales as $\langle R_g^2 \rangle \sim L^{2\nu}$, with metric exponents $\nu \simeq 3/5$ for highly supercoiled plasmids (see Fig. 2A and Fig. S1 in SI). Instead, relaxed chains display a short chain regime with $\nu \simeq 1/2$ ($M \leq 200$) and a crossover to smaller values of $\nu \simeq 0.35$ for larger chains ($M \geq 400$). These exponents suggests that relaxed plasmids in entangled solutions assume conformations similar to the ones of standard ring polymers (*38*), i.e. $\nu = 1/2$ for small $M/M_{e,linear} \lesssim 10$ and $\nu \simeq 1/3$ for large $M/M_{e,linear} \gtrsim 10$ (note that for our longest plasmids $M/M_{e,linear} \simeq 16$ hence we capture the crossover to the compact regime). On the other hand, supercoiling-driven writhing induces stronger self-interactions which are no longer screened by the neighbours (see Fig. 1B,C), in this case we thus observe a larger metric exponent ν compatible with that of a

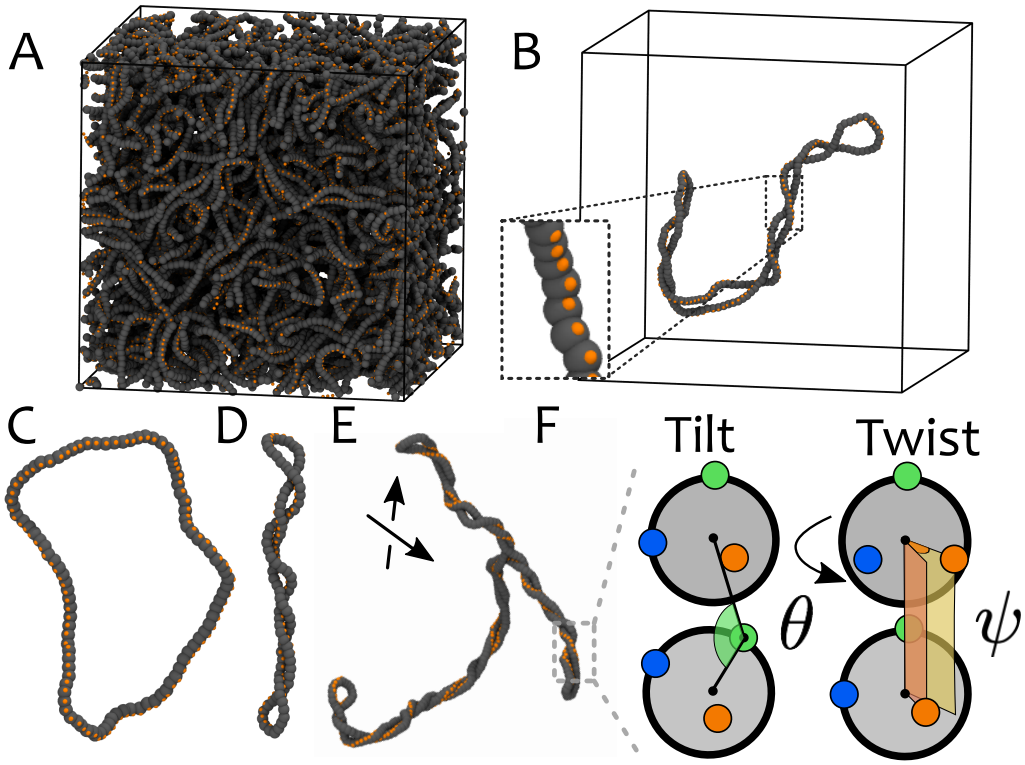

Figure 1: **A** Snapshot of simulation of entangled plasmids with length $L = 200\sigma_b \simeq 1.47$ kbp and $\sigma = 0.04$. **B** A single plasmid taken from **A** with an inset showing the patches in detail. **C-E** Snapshots of plasmids with (**C**) $\sigma = 0$, $L = 100\sigma_b \simeq 750$ bp, (**D**) $\sigma = 0.06$, $L = 100\sigma_b \simeq 750$ bp and (**E**) $\sigma = 0.06$, $L = 400\sigma_b \simeq 3$ kbp. Backbone beads are shown in grey, one set of patches are shown in orange. The other patches are not shown for clarity. **F** Sketch of tilt θ and twist ψ between consecutive beads (another angle ψ is set between blue patches, not shown). The tilt angle θ is subject to a stiff potential with equilibrium $\theta_0 = \pi$ to maintain the frame co-planar and aligned with the backbone.

self-avoiding walk. In the asymptotic limit $M \to \infty$, we expect dense systems of supercoiled plasmids to fall into the universality class of ideal (annealed) branched polymers (*39, 40*), for which $\nu = 1/3$. This is the same exponent expected for very long flexible ring polymers, although the precise folding structure will be different.

The effect of supercoiling on the average size of plasmids can be better appreciated in Fig. 2B where we show the (squared) radius of gyration rescaled by its value for relaxed plasmids and plotted against supercoiling. Importantly, it is readily apparent that for long plasmids

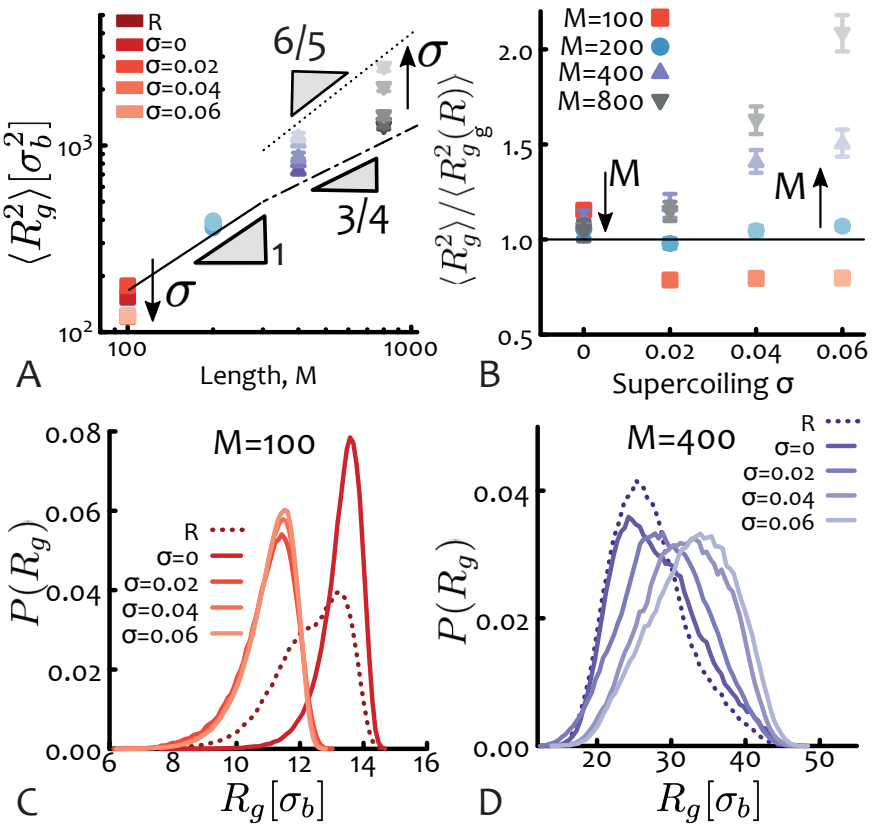

Figure 2: **Supercoiling Increases Plasmids Size in Entangled Conditions. A-B** Radius of gyrations R_g plotted against (**A**) contour length M and (**B**) supercoiling σ. Notice that for short lengths $M = 100$, increasing σ induces a collapse of the plasmids whereas for longer lengths it drives swelling. The scaling of R_g as a function of plasmid length M is compatible with that of flexible rings ($\nu = 1/2$ with crossover to $\nu \simeq 1/3$ (*38*)) and that of self-avoiding walks ($\nu = 3/5$) for relaxed and highly supercoiled plasmids, respectively. **C** The distribution of R_g for $M = 100$ is weakly bimodal showing that plasmids can be in either an "open" or a "collapsed" state. Setting a supercoiling $\sigma = 0$ stabilises the open state whereas $\sigma > 0$ induces writhing and collapse. **D** For longer plasmids ($M = 400$) larger supercoiling σ broadens the distribution and drives enlarges the average size. The unit of length is $\sigma_b = 2.5$ nm and entanglement length for linear counterparts is $M_{e,linear} = 54$ beads.

(e.g. $M \geq 400 \simeq 3$ kb) the greater the supercoiling the *monotonically* larger their typical size. We highlight that this behaviour is highly counter-intuitive as one expects supercoiling to induce a compaction of plasmids, as indeed is found computationally in dilute conditions (*32*). At the same time, supercoiled plasmids travel faster than their relaxed counterparts in gel elec-

trophoresis (*33*), due to their overall reduced size. Supercoiling is also often associated with the packaging of the bacterial genome (*10, 41*) and with organisation into topological domains in eukaryotes (*12, 13, 42*). On the contrary, here we observe a monotonic increase of R_g with supercoiling that is in marked contrast with the overall shrinking in dilute conditions (*32*) (this shrinking is recapitulated by our model when simulated in dilute conditions, see Fig. S1 in SI).

We argue that this stark difference is due to inter-chain effects and the global topological invariance of the system. Indeed, while supercoiled plasmids may want to reduce their overall size, they must also remain topologically unlinked from the neighbours. In turn, the competition between this global topological constraint and the torsional and bending rigidities appears to favour swelling of long molecules ($L > 200\sigma \simeq 1.5$ kbp) but still drives the collapse of short ones (Fig. 2B).

For the shortest plasmids considered here ($M = 100 \simeq 730bp$), we observe an interesting exception to the behaviour described above whereby the typical size is non-monotonic for increasing supercoiling levels. We attribute this peculiar behaviour to a buckling transition (see below). More specifically, for $\sigma = 0$ we find that the conformations are typically larger than the relaxed ones, but they suddenly become more collapsed for $\sigma > 0$ (Fig. 2B). [Notice that with $\sigma = 0$ we mean plasmids that are intact and torsionally constrained to have linking number deficit equal to zero. These are different from relaxed (nicked) plasmids that are not torsionally constrained as the latter do not need to obey the WFC theorem; we denote them with 'R' throughout]. We also examined the distributions of radius of gyration and noticed that relaxed short plasmids display a weakly bimodal distribution that is not found in larger plasmids (Fig. 2C,D). This bimodal distribution reflects the fact that they can be found in two typical conformational states: either open (large R_g) or more collapsed (small R_g); imposing a certain supercoiling level appears to lock the molecules in one of the two states. Since the conformational space of non-nicked plasmids must satisfy the WFC topological conservation

law, zero supercoiling ($Lk = \sigma = 0$) hinders the writhing of the plasmid because it would be energetically too costly for them to writhe multiple times with opposite sign to achieve a null global writhe, given their short length ($L/l_p = 5$). This entails that short plasmids with $\sigma = 0$ are locked into open, not self-entangled conformations. On the contrary, for $\sigma > 0$, the imposed writhing induces a conformational collapse, akin to a sharp buckling transition (*43*).

We note that the stable open state at $\sigma = 0$ for short plasmids is similar to the one computationally observed in dense solutions of semiflexible rings (*44*). These systems are expected to give rise to exotic columnar phases which would be thus intriguing to investigate in the context of dense solutions of short non-nicked plasmids with $\sigma = 0$.

We finally stress once more that the monotonic increase observed for long plasmids of their typical size with supercoiling is neither expected nor trivial and is in marked contrast with the overall shrinking behaviour found in the literature for long dilute supercoiled plasmids (*32*). Since the monomer concentration is constant for all of the systems studied, and the critical overlap concentration scales as $c^* = 3M/(4\pi R_g^3)$, one finds that c/c^* increases with supercoiling. Thus, one would naïvely expect solutions of supercoiled plasmids to be effectively more entangled than their relaxed counterparts. As a consequence, we would also expect highly supercoiled long plasmids to display reduced mobility with respect to relaxed ones.

Supercoiling Enhances DNA Mobility

We study the dynamics of entangled plasmids at different levels of supercoiling by computing the time- and ensemble-averaged mean squared displacement (TAMSD) of the centre of mass (CM) of the plasmids as $g_3(t) = \langle \boldsymbol{r}_{CM,i}(t+t_0) - \boldsymbol{r}_{CM,i}(t_0) \rangle_{i,t_0}$ (other g_i quantities are reported in Fig. S4 in SI). Curves for g_3 are shown in Fig. 3A,B for different values of plasmid supercoiling and length. Interestingly, and at odds with the findings of the previous section, we find that higher values of σ yield faster mobility especially for longer plasmids.

The diffusion coefficient of the centre of mass computed as $D_{CM} = \lim_{t\to\infty} g_3(t)/6t$ allows us to more precisely quantify how the mobility of the plasmids changes as a function of length and supercoiling. We find that while D_{CM} attains a plateau at small σ, at larger supercoiling it increases exponentially (see Fig. 3C) albeit more simulations are needed to confirm this conjecture (see below for an argument supporting the exponentially faster mobility). Additionally, we find that the diffusion coefficient as a function of plasmid length scales as $D_{CM} \sim M^{-2.2}$ and $M^{-2.45}$ for relaxed and highly supercoiled large plasmids, and are compatible with the scaling of torsionally relaxed and flexible ring polymers (*22*) (Fig. 3D). The slightly stronger dependence on plasmid length for larger supercoiling suggests that these plasmids may effectively undergo a more traditional reptation-like relaxation and for which we expect $D \sim M^{-2.4}$ (*22, 35*). As we shall see below, this conjecture is confirmed by the fact that we find most of the plasmids to display two plectonemic tips and thus preferentially assume linear-like rather than branched structures (see also SI).

We finally note that the solutions with $M = 800 \simeq 6$ kbp are not displaying a freely diffusive behaviour in spite of the fact that we ran them for more than 10^7 Brownian times (see Tab. S1 in SI); in turn, D_{CM} is overestimated as its calculation assumes free diffusion. In spite of this, values of D_{CM} for $M = 800 \simeq 6$ kbp nicely follow the general trend of the other datasets (see Fig. 3C,D).

Differential Dynamic Microscopy of DNA plasmids confirm simulations

In order to experimentally validate the prediction that supercoiling enhances the mobility of plasmids in dense solutions we perform fluorescence microscopy experiments on 3 mg/ml solutions (corresponding to a volume fraction 0.4%) made of 6-kb plasmids. We label 0.001% of the molecules in solution and use Differential Dynamic Microscopy (DDM) to determine the diffusion coefficient from videos recorded on a custom fluorescence light-sheet microscope (*46*)

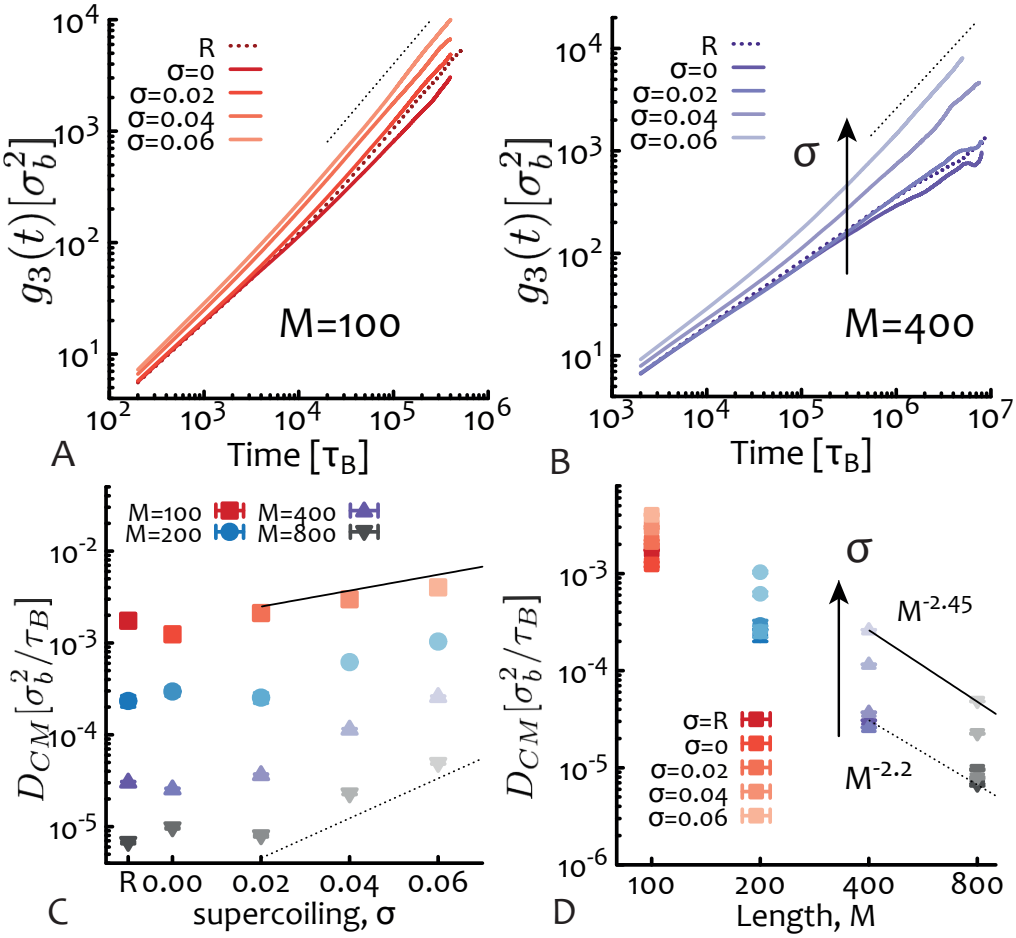

Figure 3: **Supercoiling Enhances Plasmid Mobility. A-B** Time-Averaged Mean Squared Displacement (TAMSD $= g_3$) of the plasmids for (**A**) $M = 100 \simeq 730$ bp and (**B**) $M = 400 \simeq 3$ kbp. Dotted lines are linear functions of lagtime as a guide for the eye. **C-D** Diffusion coefficient of the centre of mass $D_{CM} = \lim_{t\to\infty} g_3(t)/6t$ against (**C**) supercoiling σ and (**D**) length M. In **C** exponentials $\sim \exp(\sigma/0.05)$ (solid) and $\sim \exp(\sigma/0.02)$ (dashed) are drawn as guide for the eye (see below for a justification of exponential speed up). In **D** the best fits to the largest M for relaxed (nicked) and $\sigma = 0.06$ yield $M^{-2.2}$ and $M^{-2.45}$, respectively. Error bars are comparable to symbol size. R = "relaxed".

(Fig. 4A). DDM, as compared to single-particle tracking, allows us the measure the dynamics of the diffusing molecules without having to resolve and track individual molecules over time - optimal for DNA of this size ($R_g < 100$ nm). To pinpoint the role of supercoiling, we compare a solution of plasmids extracted from *E. coli* in the stationary phase against the same solution

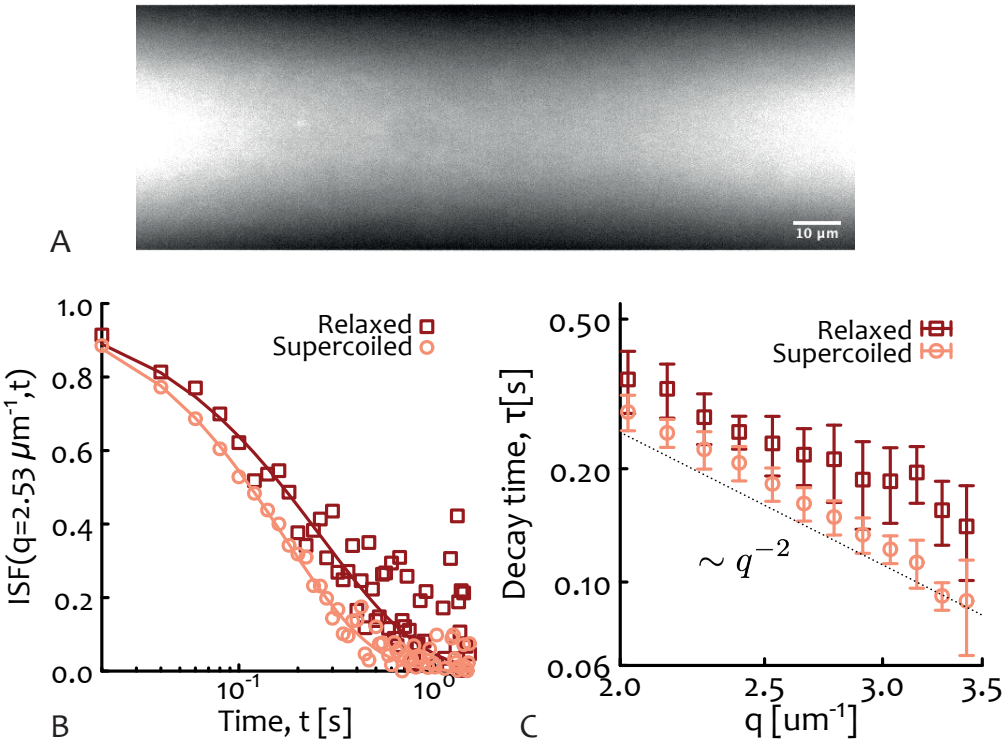

Figure 4: **DDM of Entangled Plasmid DNA Confirms the Predictions from MD Simulations.** **A** Snapshot from light-sheet microscopy showing fluorescent 5.9 kbp DNA plasmids (comparable with $M = 800$ is the MD simulations) at a concentration of 3 mg/ml concentration ($c^* \simeq 0.6$ mg/ml (*45*) and $c/c^* \simeq 5$). **B** Intermediate scattering function (ISF) obtained from DDM measurements. **C** Scaling of the ISF decay time with wave vector, showing that it scales as q^{-2}. The fitted diffusion coefficients are $D = 0.34(1)\ \mu\text{m}^2/s$ and $D = 0.44(1)\ \mu\text{m}^2/s$ for relaxed and supercoiled plasmids respectively.

pretreated with Topoisomerase I to relax the excess supercoiling (*47*) (see Methods).

As one can notice (see Fig. 4B), the intermediate scattering function (ISF) shows a faster decay for supercoiled DNA compared to relaxed circular DNA, indicating faster dynamics. We fit each ISF with a stretched exponential $f(q,t) = exp[-(t/\tau)^\gamma]$ using $\gamma \simeq 0.9-1$ to determine the decay time τ as a function of q (Fig. 4C). As shown, the decay times are well fitted by a power law $\sim q^{-2}$ that we use to extract the diffusion coefficients via the relation $\tau = (2Dq^2)^{-1}$. The resulting diffusion coefficients are $D = 0.34(1)\ \mu\text{m}^2/s$ and $D = 0.44(1)\ \mu\text{m}^2/s$ for relaxed and supercoiled solutions, respectively.

We should note that while our choice of plasmid length allows us to purify them without introducing substantial nicks ($\sim$80% are without nicks and thus supercoiled), determining their precise supercoiling level is not straightforward. In vivo, supercoiling for plasmids in the stationary phase of cell growth (the phase at which we extract our plasmids) is $\sim$2% (*48,49*). Thus, these results suggest that increasing supercoiling in solutions of entangled plasmids speeds them up and are thus in qualitative agreement with the simulations.

We should mention that while the experiments are at lower volume fraction with respect to simulations (when considering bare DNA), the buffering condition effectively thickens the diameter of DNA (*45*) thus rendering the precise comparison of experimental and simulated volume fractions difficult. We also note that due to the small size of the plasmids we are unable to accurately measure their size using single-molecule imaging. In turn, this renders the precise estimation of the overlap concentration also challenging (indirectly estimated to be about $c^* \simeq 0.6$ mg/ml (*18, 45*)). We are currently investigating alternative approaches, such as dynamic light scattering, so that in future work we can compare the intriguing predictions regarding the different sizes of supercoiled and relaxed circular DNA in dense solutions.

Supercoiling Induces a Buckling Transition in Short Plasmids

The consequence of writhing on the plasmids conformations is not captured by R_g alone (*50, 51*). Instead, it is informative to study shape descriptors which can be computed via the eigenvalues of the gyration tensor R_T (which we denote as a, b, c, with $a > b > c$ and $R_g^2 = a+b+c$). Typical shape descriptors are the asphericity (*50–52*) $a = ((a-b)^2 + (a-c)^2 + (b-c)^2)/2R_g^4$ which quantifies the deviation from a perfectly spherical arrangement and the nature of asphericity quantified by either the prolateness (see Fig. S2 in SI) or the anisotropy $an = 3(a^2 + b^2 + c^2)/(2R_g^4) - 1/2$ (shown in Fig. 5A,B). These shape descriptors reveal that for $M = 100 \simeq 730$ bp and $\sigma = 0$, plasmids are stabilised in an open, highly symmetric and oblate (M&M's) state.

Furthermore, they reveal that these short plasmids undergo a buckling transition to a closed, asymmetric and prolate (rugby ball) shape for $\sigma > 0$. The sharp first-order-like buckling transition (see Fig. 5A and SI) is weakened for larger contour lengths (see Fig. 5B), as self-writhing is energetically allowed even for $\sigma = 0$ (negative and positive self-crossings must cancel each other to satisfy the WFC conservation law). At the same time, both short and long plasmids display a general increase in asphericity, prolateness and anisotropy with increasing supercoiling, strongly suggesting that the plasmids assume elongated and double-folded conformations (see Fig. S2 in SI).

Supercoiling Decreases the Spanning Minimal Surface

It is natural to associate the open-oblate/closed-prolate conformations assumed by DNA plasmids to a larger/smaller (minimal) spanning area, respectively (*53*). The size of this area may be relevant for the dynamics because it could be "threaded" by neighbouring plasmids hence hindering the dynamics (*24, 54, 55*). To quantify this in more detail we calculated the minimal surface (*53*) using the algorithm in Refs. (*55, 56*) for flexible ring polymers. We found that the minimal area grows approximately linearly with the plasmids' contour, as expected for $\nu \leq 1/2$ (*55*) (Fig. 5C). Importantly, we also observed that it overall decreased with supercoiling with the notable exception of short $M \leq 200 \simeq 1.5$ kbp plasmids, for which there is a small increase for $\sigma = 0$ with respect to the relaxed case, again confirming the "topological locking" of open conformations (Fig. 2A).

A crude way to estimate the decrease in "threadable" area of a plasmid Σ is via recursive bisections of a perfect circle into several connected smaller circles joined at a vertex mimicking writhe-induced self-crossing. Each time a circle is split into two smaller ones the new radii are $R' \simeq R/2$ and thus n circles (with $n-1$ self-crossings) have radii $R' = R/n$ yielding an overall spanning surface $\Sigma \simeq n\pi(R/n)^2 \sim 1/n \sim 1/\sigma$. The same scaling of the thread-

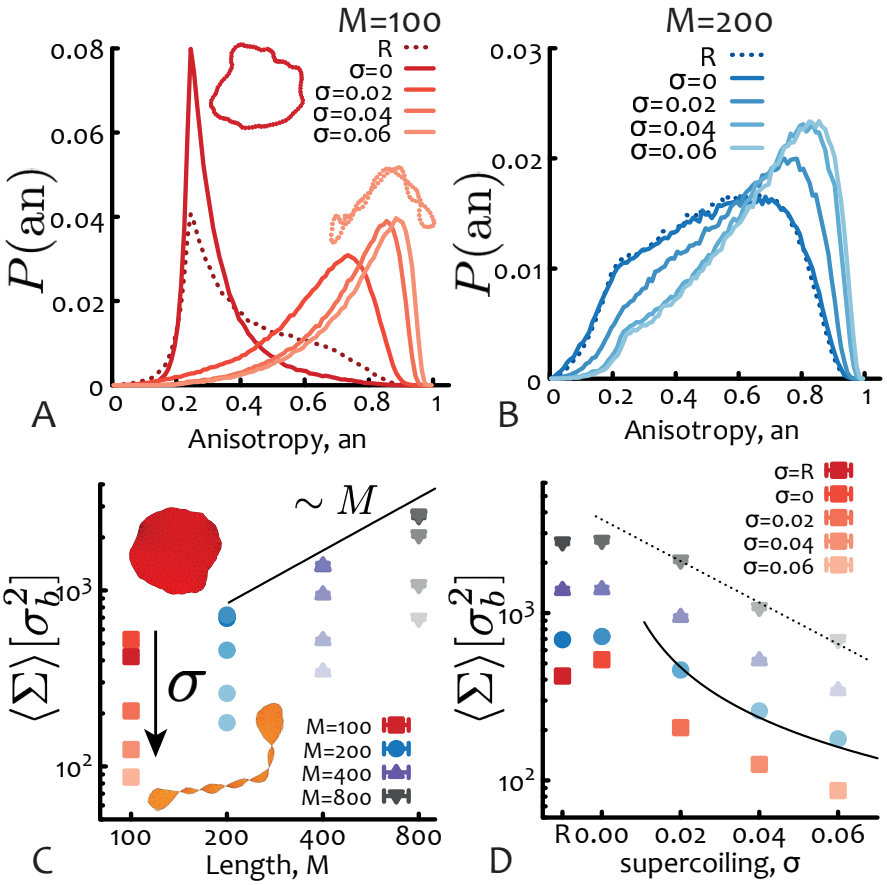

Figure 5: **Supercoiling Induces Buckling in Short Plasmids and Reduces the Threadable Area. A** The anisotropy shape descriptor (an, see text) for short plasmids $M = 100 \simeq 730$ bp displays a sharp buckling transition between an open and roughly symmetric state for $\sigma = 0$ and a collapsed and anisotropic one for $\sigma > 0$. In inset, two examples of conformations are shown. **B** For longer plasmids ($M \geq 200 \simeq 1.5$ kbp) supercoiling shifts the anistropy to larger values indicating a smoother transition to more prolate conformations. **C** Scaling of the average minimal surface size $\langle\Sigma\rangle$ as a function of plasmids length (solid line shows the linear scaling). In inset, two examples of surfaces for $M = 100 \simeq 730$ bp are shown. **D** The size of the minimal surface area monotonically decreases with supercoiling (with the exception of short $M \leq 200 \simeq 1.5$ kbp plasmids). The solid and dashed lines scale as $1/\sigma$ and $e^{-\sigma/0.035}$, respectively, and are drawn as a guide for the eye. R = "relaxed". The unit of length is $\sigma_b = 2.5$ nm. The error bars, typically smaller than the symbol size, represent the error of the mean area.

able area is obtained if one considers the supercoil as if wrapped around a cylinder of radius r (*57*) and projected in 2D; in this case, one would find that the enclosed area in each of the

n superhelix turns is about $rL_{ee}/(n-1)$, where L_{ee} is the end-to-end length of the plasmid. Given that $r \sim 1/\sigma$ (*57*) and that L_{ee} is expected to be insensitive on σ for large supercoiling (see also Fig. 2B showing plateauing of R_g for $M \leq 400$), one finds a total threadable area scaling as $\Sigma \simeq nrL_{ee}/(n-1) \sim 1/\sigma$. The fact that our data is instead more compatible with an exponential decrease of Σ as a function of supercoiling (Fig. 5D) suggests that the approximation of the supercoil wrapped around a cylinder may not be accurate. In fact, considering the large persistence length of DNA, it may be thermodynamically preferred to flatten and shrink the many inner openings at the expense of storing longer contour length at the fewer tips (see also snapshots in Fig. 1B-E and inset of Fig. 5C). These estimations are in good agreement with the scaling of the minimal surface, although we cannot rule out other functional forms (for instance exponential, see Fig. 5D). [Note that the so-called magnetic moment and radius (*58*) give similar results albeit different scaling (see Fig. S3 in SI)].

Supercoiling Reduces Threadings

Motivated by the observation that the minimal surface – or "threadable area" – sharply decreases with supercoiling, we decided to quantify more precisely the number of threadings per plasmid for different levels of supercoiling. To this end we identify a plasmid to be "passively threaded" by another when the minimal surface of the former is intersected by the contour of the latter (at least twice, as they are topologically unlinked) (*55*) (Fig. 6A). As shown in Fig. 6B, the average number of threadings per plasmid $\langle n_t \rangle$ also appears to decrease exponentially with supercoiling and to mirror the behaviour of the mean threadable area $\langle \Sigma \rangle$. [As for the minimal surface Σ, a notable exception to this general trend is the case of short plasmids ($M = 100$) for which we find that $\langle n_t \rangle$ is statistically larger for $\sigma = 0$ than for relaxed plasmids because of the "topological locking" that we explained above.]

Based on these findings, we can also advance an argument as for why the diffusion co-

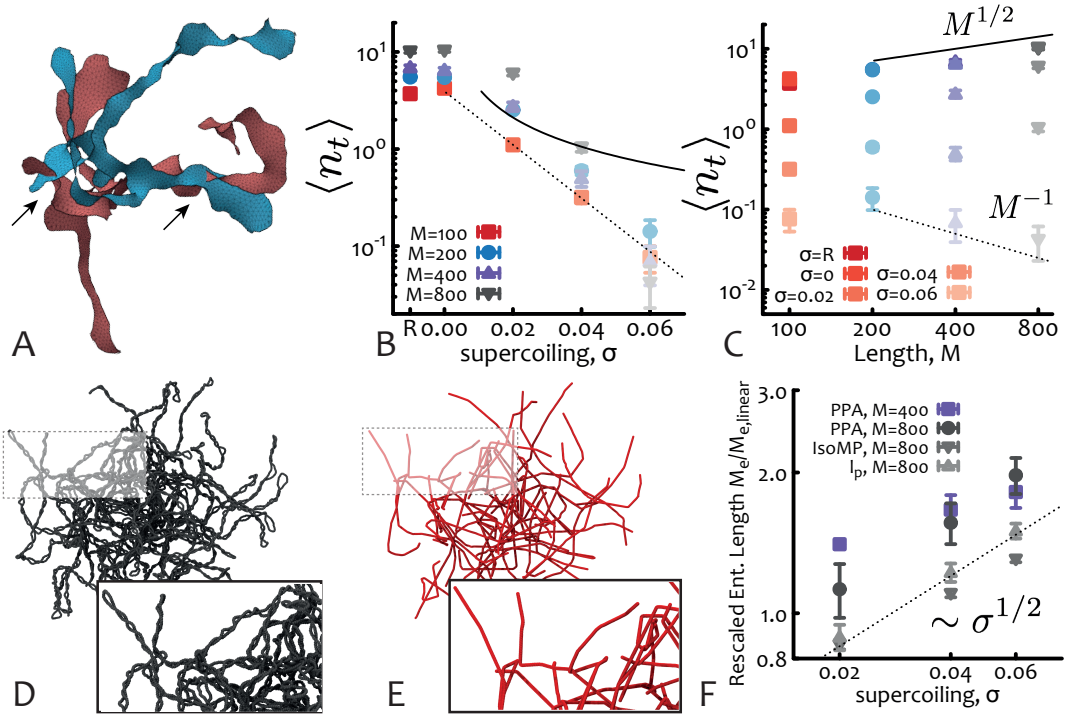

Figure 6: **Supercoiling Reduces Threadings and Entanglements. A** Snapshot of two threading plasmids (relaxed, $M = 800 \simeq 6$ kbp) with minimal surfaces drawn and intersections highlighted by arrows. **B** Number of threadings per plasmid as a function of supercoiling (dashed=exponential, solid=$1/\sigma$). **C** Number of threadings per plasmid as a function of DNA length (dashed=$1/M$, solid=$M^{1/2}$). **D,E** Snapshots of the PPA analysis run on a system with plasmids $M = 800 \simeq 6$ kbp and $\sigma = 0.06$. **F** The effective entanglement length increases with supercoiling as $M_e/M_{e,linear} \sim \sigma^{\alpha}$ with $\alpha \simeq 0.5$ for both PPA and IsoMP methods. Note that $M_{e,linear} = 54 \pm 2$ (PPA) and $M_{e,linear} = 49 \pm 2$ (IsoMP). The effective persistence length $l_p/l_{p,linear}$ also shows a scaling compatible with $\sigma^{1/2}$ ($l_{p,linear} = 18 \pm 1$).

efficient of plasmids increases exponentially with supercoiling: Recent evidence suggest that the dynamics of ring polymers with threadings slow down exponentially with the number of threadings (e.g., entangled rings (*55, 59, 60*), melts of tadpole-shaped polymers (*20, 61*) or compressed long plasmids (*62*)). We thus expect the dynamics of highly supercoiled (threading-poor) plasmids to be exponentially faster than their relaxed (threading-rich) counterparts, as seen in Fig. 3C.

Intriguingly, in the case of short plasmids in which setting $\sigma = 0$ increases the threadable

area and also the number of threadings, we also find a slower dynamics, in full agreement with our argument (see Figs. 6B and 3C).

Supercoiling Reduces Entanglements

The shape descriptors studied above suggest that long plasmids assume prolate double-folded conformations, but it remains unclear whether the conformations are simply plectonemic (linear-like) or more branched into comb, star or tree-like structures (*63*). We thus computed the local absolute writhe along the contour length, $W(s)$, from which the number and location of plectonemic tips can be identified as the local maxima of $W(s)$ (*64, 65*) (see Methods and SI). This calculation reveals that most of the conformations with $\sigma \geq 0.04$ have 2 tips and so are mainly linear-like plectonemic conformations (see Fig. S5 in SI). [For smaller supercoiling it is difficult to unambiguously distinguish tips from other regions of large curvature.]

In light of this finding another apparent controversy arises. Indeed, arguably, linear chains half the length as their ring counterparts are expected to diffuse slower than the rings due to reptation relaxation induced by ordinary entanglements (assuming that the entanglement length is the same for the two systems) (*22*); instead, we observe the opposite trend. To explain this result we adapted the primitive path analysis (*66*) (PPA) and isoconfigurational mean path (*67*) (IsoMP) methods to estimate the effective entanglement length of these systems (see Fig. 6C,D and SI Fig. S10). For PPA, we determined an effective entanglement length M_{e} by leveraging the fact that the tips of linear-like or branched conformations represent effective termini that can be pinned in space (see SI for more details on PPA and IsoMP methods). [Note that the PPA method typically fails for standard flexible ring polymers because there are no well-defined ends to pin].

We find that irrespective of the method chosen, the scaling of the effective entanglement length is compatible with $M_e \sim \sigma^{1/2}$ (Fig. 6F), suggesting that the larger the supercoiling

the less entangled the plasmids. [The numerical difference of PPA and IsoMP is a known feature for topologically constrained ring polymers (*67, 68*) with $M_{e,PPA}/M_{e,IsoMP} \simeq 3/2$ and is in agreement with our findings for plasmids.] We argue that this effective reduction in entanglement (opposite to what one would naively expect considering $c/c^* \sim R_g^3/M$ or similar packing length arguments as $p = 1/(\rho_{\text{chain}} L_{ee}^2)$, L_{ee} being the end-to-end distance) is due to the fact that supercoiling (i) induces highly anisotropic conformations and (ii) it increases the local concentration of intra-chain beads (*69*). Indeed, since the superhelix radius of plasmids scales as $r \sim 1/\sigma$ (*57*) and most plasmids display only two tips (see SI Fig. S6), this entails that the intra-chain density $\rho_{intra} \sim M/V \sim \sigma^2$, (with $V = \pi r^2 L_{ee}$ the approximated cylindrical volume of the supercoil) grows with sigma.

Notably, we also find that the effective persistence length, computed as the decay length of the tangent-tangent correlation, $c_t = \exp(-l/l_p^*)$, along the plasmid backbone (from tip to tip) scales as $l_p^* \sim \sigma^{1/2}$, in turn yielding $M_e \sim l_p^*$ or $M_e \sim l_k^*$ (Fig. 6F). This is compatible with the fact that our systems appear to be at the crossover between the semiflexible and stiff regimes, based on the values of density, stiffness and chain diameter and as supported by the typical values of M_e extracted from both PPA and IsoMP, which are of the order of the effective Kuhn length $l_k^* \simeq 2l_p^*$ (Fig. 6F). In this crossover, both tube diameter and entanglement length scale linearly with the Kuhn length l_k (*70*). The stiffening of the supercoiled plasmids can be naturally thought of as due to the self-writhing; in particular, one may argue that the shorter the contour length between self-crossings, i.e. the smaller $1/\sigma$, the longer the effective persistence length displayed by the plasmids. A Flory-type estimate of the interaction free energy of n monomers $F_{int} \sim kTvn^2/r^3$, per superhelix turn ($n \sim \sigma^{-1}$ and $r \sim \sigma^{-1}$) gives $F_{int} \sim \sigma$. This can be viewed as if the excluded volume of the cylindrical Kuhn monomer v (composed of l_k^*/d spherical beads in line) grew by a factor of σ. Since $v \sim (l_k^*)^2 d$ (*71*), the effective length Kuhn length $l_k^* \sim \sigma^{1/2}$.

Then, in the stiff regime, the plasmids behave as if they were rigid chains of diameter $2r \sim 2/\sigma$ confined within narrow tubes with diameter a; in analogy with the classical Odijk problem (*72*) we can thus write $M_e = a^{2/3} l_k^{1/3}$. In turn, the value of the tube diameter can be obtained from the estimate that in each area element aM_e spanned by the plasmid, there is about 1 transversal segments, i.e. $\rho_s a M_e \simeq 1$ with $\rho_s = \phi/(2r)^2$ the arclength density and ϕ the polymer volume fraction ($\phi = r^3 M(b/r)/V$ in terms of supercoil turns with $r \sim b/\sigma$). Combining these together (*70*) we expect $M_e \simeq l_k \phi^{-2/5} \left(d/l_k\right)^{4/5} \sim \sigma^{0.1}$, to be attained at very large values of σ, for which the stiff regime ($a \ll M_e$ and $l_k \ll M_e$) is justified.

Finally, we note that for short plasmids the PPA method cannot identify an entanglement length, confirming that these are very poorly entangled in the standard sense. As such, their dynamics are mostly determined by threadings, which are abundant also in short plasmids (see Fig. 6B,C).

Discussion

In this work we have studied the dynamics of entangled solutions of DNA plasmids to understand how supercoiling can be leveraged to tune the rheology of dense DNA solutions orthogonally to other traditional methods, such as varying length or concentration. We have discovered that, contrary to what is typically assumed, the size of long plasmids increases with supercoiling when in entangled solutions.

In dilute conditions, supercoiled plasmids are expected to fall into the universality class of interacting annealed branched polymers for which a metric exponent $\nu = 7/13$ is expected asymptotically (*39, 63*). In the melt phase, the self-interactions are screened and we thus expect supercoiled plasmids to behave as ideal annealed branched polymers or lattice animals for which $\nu = 1/4$ (*40*); being unphysical in $d = 3$, we expect the size of very large supercoiled plasmids in the melt to scale with a metric exponent $\nu = 1/3$. Although this is the same scaling

expected for relaxed rings (*23,73*) the folded structures are expected to be different. Importantly, the supercoiling-driven swelling can still be achieved through a non-universal prefactor in front of a supercoiling independent universal scaling $M^{1/3}$, for instance due to an effectively larger persistence length (as we found in this work, Fig. 6F). The fact that we observe a metric exponent that depends on σ (Fig. 2A) thus suggests that our simulations are not in the asymptotic limit, and yet still in a regime that is experimentally interesting.

Surprisingly, we find the swelling of supercoiled plasmids is mirrored by an enhanced mobility. Our predictions are supported by experiments which show that the diffusion coefficient of entangled intact and supercoiled ($\sigma \simeq 0.02$) plasmids is larger than that of relaxed ones, i.e. with $\sigma \simeq 0$. We discovered that this enhanced mobility is due to severely asymmetric conformations which greatly reduce the threadable area and number of threadings. In parallel, entanglements are also reduced as supercoiling increases the effective entanglement length by increasing the local concentration of intra-chain contacts. We note that threadings are abundant also in short plasmids (Fig. 6B) that are poorly entangled in the standard sense; we observe that in this case threadings play a major role in determining the dynamics of short plasmids (notably for $M = 100$, the case with $\sigma = 0$ is slower and displays more threadings than the relaxed one). We have thus discovered that the unexpected enhanced diffusivity of entangled supercoiled DNA is due to a combination of reduced entanglements and, in particular, threadings.

We conjecture that beyond the range of lengths studied in this work ($0.7 - 6$ kbp), supercoiled plasmids in entangled solutions may display branched and annealed conformations (i.e. with non-fixed branching points), triggering the need of arm retraction or plectoneme diffusion/hopping relaxation mechanisms. These processes are notoriously slow, on the order of kbp^2/s (*74*), and we thus predict a re-entrant slowing down of the diffusion of supercoiled plasmids. Indeed, they ought to behave as quenched/annealed branched polymers on timescales shorter/longer than plectoneme diffusion, respectively. Ultimately, in spite of the expected onset

of (exponentially) slowly diffusive "branched-polymer-like" regime for supercoiled plasmids, relaxed ones will still display many more threadings,which we argue will still (exponentially) slow down their dynamics also in the large length limit. Dissecting the contribution of these mechanisms will require longer simulations than currently possible.

In summary, our results suggest a route for the topological tuning of the rheology of DNA-based complex fluids that employs supercoiling as a mean to control DNA mobility. We note that the fact that supercoiling regulates the number of threadings per plasmids can also be leveraged in polydisperse systems or in blends of linear and supercoiled DNA or other biopolymer composites, where threading of rings by the linear fraction is key to determine the stress relaxation of the fluids (*20, 21, 61, 75*).

In the future, it would be interesting to further investigate longer plasmids with selected or varying levels of supercoiling. Albeit experimentally difficult, this may be feasible using caesium chloride gradient separation techniques (*76*). Ultimately, understanding how DNA topology and supercoiling affect the dynamics and conformational properties of plasmids in *entangled* or *crowded* conditions may not only reveal novel pathways to finely tune the rheology of complex biopolymer fluids but also shed light on the role of supercoiling on chromosome dynamics in vivo (*10, 77*).

Material and Methods

Molecular Dynamics

Each bead in our simulation is evolved through the Langevin equation $m_a \partial_{tt} \vec{r}_a = -\nabla U_a - \gamma_a \partial_t \vec{r}_a + \sqrt{2 k_B T \gamma_a} \vec{\eta}_a(t)$, where m_a and γ_a are the mass and the friction coefficient of bead a, and $\vec{\eta}_a$ is its stochastic noise vector satisfying the fluctuation-dissipation theorem. U is the sum of the energy fields (see SI). The simulations are performed in LAMMPS (*36*) with $m = \gamma = k_B = T = 1$ and using a velocity-Verlet algorithm with integration time step $\Delta t = 0.002\,\tau_B$,

where $\tau_B = \gamma\sigma^2/k_BT \simeq 0.03$ μs is the Brownian time ($\gamma = 3\pi\sigma\eta_w$ with $\eta_w = 1$ cP the viscosity of water).

Branching Analysis

Following Refs. (*64, 78*), we compute the absolute writhe of a segment of a plasmid as $W(s) = (1/4\pi)\int_{s-l}^{s}\int_{s}^{s+l}|(\boldsymbol{r}_1-\boldsymbol{r}_2)\cdot(d\boldsymbol{r}_1\times d\boldsymbol{r}_2)/|\boldsymbol{r}_1-\boldsymbol{r}_2|^3|$ with window $l = 50$ beads. This calculation yields a function $W(s)$ whose maxima represent regions of high local writhe and can identify tips of plectonemes. In addition to being a local maximum, we require that $W(s) > 0.35$ to avoid false positives. See SI for more details.

Primitive Path Analysis

Following Ref. (*66*), we fix certain polymer segments in space, turn intra-chain repulsive interactions off and keep inter-chain interactions on. We then run simulations at low temperature 0.01 to find a ground state. The resulting chain conformations (primitive paths) are made of straight segments connected by sharp kinks due to entanglements. The entanglement length is then given by $N_e = r_{\text{ee}}^2/(Mb_{pp}^2)$, where r_{ee} is the mean endpoint distance, M is the number of monomers between the fixed points and b_{pp} is the mean bond-length of the primitive path. We adapt the classical PPA for plasmids by fixing the tips of all detected plectonemes instead of the end points of linear chains (see SI).

DNA preparation

Double-stranded 5.9 kbp DNA plasmids are replicated in E. coli, collected at the onset of stationary phase, before being extracted and purified using our previously described protocols (*45*). Following purification the DNA solution is $\sim$80% supercoiled and $\sim$20% relaxed circular, as determined from gel electrophoresis (see SI, Fig. S6). To produce concentrated solutions of relaxed circular DNA, Topoisomerase I (New England Biolabs) is used to convert the DNA

topology from supercoiled to relaxed circular (*79*) (see SI, Fig. S6). Both supercoiled and relaxed circular DNA solutions are concentrated to 3 mg/ml using an Eppendorf Vacufuge 5301.

Fluorescence Imaging

To visualize DNA diffusion in concentrated solutions, supercoiled or relaxed circular DNA is labeled with YOYO-1 dye (Thermo Fisher Scientific) at a 4:1 base pair:dye ratio, and added at a concentration of 0.045 μg/ml to 3 mg/ml solutions of supercoiled or relaxed circular DNA described above. Glucose (0.9 mg/ml), glucose oxidase (0.86 mg/ml), and catalase (0.14 mg/ml) are added to inhibit photobleaching (*47, 80*). The DNA solutions are pipetted into capillary tubing that is index-matched to water and imaged using a custom-built light-sheet microscope with a 488 nm excitation laser, an excitation objective of 10x 0.25 numerical aperture (NA), an imaging objective of 20x 1.0 NA, and an Andor Zyla 4.2 CMOS camera. At least 4 sample videos are recorded at 50 frames per second for 2000 frames. The video dimensions are 256 x 768 pixels, which are then analyzed by examining regions of interest (ROI) of 256 x 256 pixels (50 x 50 μm).

DDM analysis

We follow methods previously described to investigate DNA diffusion using Differential Dynamic Microscopy (DDM) (*46*). Briefly, from each ROI we obtain the image structure function or DDM matrix $D(q, \Delta t)$, where q is the magnitude of the wave vector and Δt is the lag time. To extract the transport dynamics of the diffusing DNA molecules, we fit the structure functions to $D(q, \Delta t) = A(q)[1 - f(q, \Delta t)] + B(q)$, where B is a measure of the camera noise, A depends on the optical properties of both the sample and microscope, and $f(q, \Delta t)$ is the intermediate scattering function (ISF). Based on our previous studies of microspheres and DNA diffusing in crowded environments, we fit the ISFs to stretched exponentials of the form

$f(q, \Delta t) = \exp -(\Delta t/\tau(q))^{\gamma(q)}$, where τ is the characteristic decay time and γ is the stretching exponent, both of which depend on q (*47*).

For normal free diffusion, one expects ISFs described by a simple exponential, i.e., $\gamma = 1$, while our scattering functions are better fitted with stretching exponents between $0.9-1$. Having extracted the decay times of density fluctuations τ over a range of spatial frequencies q, we fit the results to $\tau = (2Dq^2)^{-1}$ to determine the diffusion coefficient, D, for the DNA plasmids.

References

1. S. H. Um, *et al.*, *Nat. Mater.* **5**, 797 (2006).

2. P. W. K. Rothemund, *Nature* **440**, 297 (2006).

3. N. C. Seeman, H. F. Sleiman, *Nat. Rev. Mater.* **3**, 1 (2017).

4. C. Mao, W. Sun, N. C. Seeman, *Nature* **386**, 137 (1997).

5. M. E. Leunissen, *et al.*, *Soft Matter* **5**, 2422 (2009).

6. A. Bates, A. Maxwell, *DNA topology* (Oxford University Press, 2005).

7. R. M. Robertson, D. E. Smith, *Proc. Natl. Acad. Sci. USA* **104**, 4824 (2007).

8. R. E. Teixeira, A. K. Dambal, D. H. Richter, E. S. G. Shaqfeh, S. Chu, *Macromolecules* **40**, 3514 (2007).

9. R. Fitzpatrick, *et al.*, *Phys. Rev. Lett.* **121**, 257801 (2018).

10. F. Wu, *et al.*, *Nature Communications* **10**, 1 (2019).

11. D. Racko, F. Benedetti, D. Goundaroulis, A. Stasiak, *Polymers (Basel).* **10**, 1 (2018).

12. F. Benedetti, J. Dorier, Y. Burnier, A. Stasiak, *Nucleic Acids Res.* **42**, 2848 (2014).

13. C. Naughton, *et al.*, *Nat. Struct. Mol. Biol.* **20**, 387 (2013).

14. R. N. Irobalieva, *et al.*, *Nat. Commun.* **6**, 1 (2015).

15. Y. A. G. Fosado, D. Michieletto, D. Marenduzzo, *Phys. Rev. Lett.* **119**, 1 (2017).

16. T. Sutthibutpong, *et al.*, *Nucleic Acids Res.* **44**, 9121 (2016).

17. Y. Ding, *et al.*, *Proc. Natl. Acad. Sci. USA* **111**, 15402 (2014).

18. S. Laib, R. M. Robertson, D. E. Smith, *Macromolecules* **39**, 4115 (2006).

19. X. Zhu, B. Kundukad, J. R. Van Der Maarel, *J. Chem. Phys.* **129**, 1 (2008).

20. A. Rosa, J. Smrek, M. S. Turner, D. Michieletto, *ACS Macro Letters* **9**, 743 (2020).

21. M. Kapnistos, *et al.*, *Nat. Mater.* **7**, 997 (2008).

22. J. D. Halverson, W. B. Lee, G. S. Grest, A. Y. Grosberg, K. Kremer, *J. Chem. Phys.* **134**, 204905 (2011).

23. A. Rosa, R. Everaers, *Phys. Rev. Lett.* **112**, 118302 (2014).

24. D. Michieletto, M. S. Turner, *Proc. Natl. Acad. Sci. USA* **113**, 5195 (2016).

25. B. A. Krajina, A. Zhu, S. C. Heilshorn, A. J. Spakowitz, *Phys. Rev. Lett.* **121**, 148001 (2018).

26. Q. Wu, *et al.*, *Science* **358**, 1434 (2017).

27. P. M. Rauscher, K. S. Schweizer, S. J. Rowan, J. J. De Pablo, *Macromolecules* **53**, 3390 (2020).

28. B. Mei, Z. E. Dell, K. S. Schweizer, *Macromolecules* **53**, 10431 (2020).

29. L. R. Gómez, N. A. García, T. Pöschel, *Proceedings of the National Academy of Sciences of the United States of America* **117**, 3382 (2020).

30. M. Abadi, M. F. Serag, S. Habuchi, *Nat. Commun.* **9** (2018).

31. C. A. Brackley, A. N. Morozov, D. Marenduzzo, *J. Chem. Phys.* **140**, 135103 (2014).

32. B. A. Krajina, A. J. Spakowitz, *Biophys J.* **111**, 1339 (2016).

33. J. Cebrián, *et al.*, *Nucleic Acids Res.* **3112**, 1 (2014).

34. M. Doi, S. Edwards, *The theory of polymer dynamics* (Oxford University Press, 1988).

35. K. Kremer, G. S. Grest, *J. Chem. Phys.* **92**, 5057 (1990).

36. S. Plimpton, *J. Comp. Phys.* **117**, 1 (1995).

37. M. R. Dennis, J. H. Hannay pp. 3245–3254 (2005).

38. J. D. Halverson, W. B. Lee, G. S. Grest, A. Y. Grosberg, K. Kremer, *J. Chem. Phys.* **134**, 204904 (2011).

39. A. M. Gutin, A. Y. Grosberg, E. I. Shakhnovich, *Macromolecules* **26**, 3598 (1993).

40. T. C. Lubensky, J. Isaacson, *Phys. Rev. A* **20**, 2130 (1979).

41. R. R. Sinden, D. E. Pettijohn, *Proceedings of the National Academy of Sciences of the United States of America* **78**, 224 (1981).

42. F. Benedetti, D. Racko, J. Dorier, Y. Burnier, A. Stasiak, *Nucleic Acids Res.* **45**, 9850 (2017).

43. K. Ott, L. Martini, J. Lipfert, U. Gerland, *Biophysical Journal* **118**, 1690 (2020).

44. M. Bernabei, P. Bacova, A. J. Moreno, A. Narros, C. N. Likos, *Soft Matter* **9**, 1287 (2013).

45. R. M. Robertson, S. Laib, D. E. Smith, *Proc. Natl. Acad. Sci. USA* **103**, 7310 (2006).

46. R. Cerbino, V. Trappe, *Phys. Rev. Lett.* **100**, 188102 (2008).

47. D. M. Wulstein, K. E. Regan, J. Garamella, R. J. McGorty, R. M. Robertson-Anderson, *arXiv* (2019).

48. V. L. Balke, J. D. Gralla, *Journal of bacteriology* **169**, 4499 (1987).

49. Z. Wang, P. Dröge, *Journal of Molecular Biology* **271**, 499 (1997).

50. E. J. Rawdon, *et al.*, *Macromolecules* **41**, 8281 (2008).

51. F. Benedetti, *et al.*, *Nucleic Acids Res.* **43**, 2390 (2015).

52. A. Rosa, E. Orlandini, L. Tubiana, *Macromolecules* **44**, 8668 (2011).

53. M. Lang, *Macromolecules* **46**, 1158 (2013).

54. D. Michieletto, N. Nahali, A. Rosa, *Phys. Rev. Lett.* **119**, 197801 (2017).

55. J. Smrek, A. Y. Grosberg, *ACS Macro Lett.* **5**, 750 (2016).

56. J. Smrek, K. Kremer, A. Rosa, *ACS Macro Lett.* **8**, 155 (2019).

57. T. C. Boles, J. H. White, N. R. Cozzarelli, *Journal of Molecular Biology* **213**, 931 (1990).

58. R. D. Schram, A. Rosa, R. Everaers, *Soft Matter* **15**, 2418 (2019).

59. D. Michieletto, D. Marenduzzo, E. Orlandini, G. P. Alexander, M. S. Turner, *Soft Matter* **10**, 5936 (2014).

60. J. Smrek, I. Chubak, C. N. Likos, K. Kremer, *Nature Communications* **11**, 1 (2020).

61. Y. Doi, A. Takano, Y. Takahashi, Y. Matsushita, *Macromolecules* **48**, 8667 (2015).

62. B. W. Soh, A. R. Klotz, R. M. Robertson-Anderson, P. S. Doyle, *Phys. Rev. Lett.* **123**, 048002 (2019).

63. R. Everaers, A. Y. Grosberg, M. Rubinstein, A. Rosa, *Soft Matter* (2017).

64. D. Michieletto, *Soft Matter* **12**, 9485 (2016).

65. A. V. Vologodskii, S. D. Levene, K. V. Klenin, M. Frank-Kamenetskii, N. R. Cozzarelli, *Journal of Molecular Biology* **227**, 1224 (1992).

66. R. Everaers, *et al.*, *Science (80-.).* **303**, 823 (2004).

67. W. Bisbee, J. Qin, S. T. Milner, *Macromolecules* **44**, 8972 (2011).

68. R. S. Hoy, M. Kröger, *Phys. Rev. Lett.* **124**, 147801 (2020).

69. A. V. Vologodskii, N. R. Cozzarelli, *J. Mol. Biol.* **227**, 1224 (1992).

70. S. T. Milner, *Macromolecules* **53**, 1314 (2020).

71. M. Rubinstein, H. R. Colby, *Polymer physics*, no. 2003 (1995).

72. T. Odijk, *Macromolecules* **16**, 1340 (1983).

73. A. Y. Grosberg, Y. Rabin, S. Havlin, A. Neer, *EPL (Europhysics Lett.* **23**, 373 (1993).

74. M. T. Van Loenhout, M. V. De Grunt, C. Dekker, *Science* **338**, 94 (2012).

75. D. Parisi, J. Ahn, T. Chang, D. Vlassopoulos, M. Rubinstein, *Macromolecules* **53**, 1685 (2020).

76. D. B. Clewell, D. R. Helinski, *Proceedings of the National Academy of Sciences of the United States of America* **62**, 1159 (1969).

77. A. Japaridze, C. Gogou, J. W. Kerssemakers, H. M. Nguyen, C. Dekker, *Nature Communications* **11**, 1 (2020).

78. K. Klenin, J. Langowski, *Biopolymers* **54**, 307 (2000).

79. C. Chapman, S. Shanbhag, D. E. Smith, R. M. Robertson, *Soft Matter* **8**, 9177 (2012).

80. J. Garamella, K. Regan, G. Aguirre, R. J. McGorty, R. M. Robertson-Anderson, *Soft Matter* **16**, 6344 (2020).

81. T. Ge, S. Panyukov, M. Rubinstein, *Macromolecules* **49**, 708 (2016).

82. D. Michieletto, T. Sakaue, *ACS Macro Letters* pp. 129–134 (2021).

Acknowledgments

The authors would like to acknowledge the networking support by the "European Topology Interdisciplinary Action" (EUTOPIA) CA17139. This project has received funding from the European Union's Horizon 2020 programme under grant agreement No. 731019 (EUSMI). DM acknowledges the computing time provided on the supercomputer JURECA at Jülich Supercomputing Centre, support by the Leverhulme Trust (ECF-2019-088), the Royal Society and ERC (StG TAP 947918). JS acknowledges the support from the Austrian Science Fund (FWF) through the Lise-Meitner Fellowship No. M 2470-N28. JS is grateful for the computational time at Vienna Scientific Cluster. Sample codes can be found at git.ecdf.ed.ac.uk/dmichiel/supercoiledplasmids.

Competing interests: The authors declare that they have no competing interests. **Data and materials availability:** All data needed to evaluate the conclusions in the paper are present in the paper and/or the Supplementary Materials.

Supplementary materials

Materials and Methods

Supplementary Text

Figs. S1 to S11

Tables S1

Topological Tuning of DNA Mobility in Entangled Solutions of Supercoiled Plasmids. Supplementary Information

Jan Smrek[1], Jonathan Garamella[2],
Rae Robertson-Anderson[2], Davide Michieletto[3,4,*]

[1]Faculty of Physics, University of Vienna, Boltzmanngasse 5, A-1090 Vienna, Austria
[2]Department of Physics and Biophysics, University of San Diego
San Diego, CA 92110, USA
[3]School of Physics and Astronomy, University of Edinburgh
Peter Guthrie Tait Road, Edinburgh, EH9 3FD, UK
[4]MRC Human Genetics Unit, Institute of Genetics and Molecular Medicine
University of Edinburgh, Edinburgh EH4 2XU, UK
[*]To whom correspondence should be addressed; E-mail: davide.michieletto@ed.ac.uk

MD simulations

DNA is represented as a twistable elastic chain (as detailed in Ref. (*31*)) whereby the backbone is made of beads each decorated by three patches (please refer to Fig. 1 in the main text).The backbone beads interact via a purely repulsive Lennard-Jones potential as

$$U_{\rm LJ}(r) = \begin{cases} 4\epsilon\left[\left(\frac{\sigma_b}{r}\right)^{12} - \left(\frac{\sigma_b}{r}\right)^{6} + \frac{1}{4}\right] & r \leq r_c \\ 0 & r > r_c \end{cases}, \tag{1}$$

where r denotes the separation between the bead centers. The cutoff distance $r_c = 2^{1/6}\sigma$ is chosen so that only the repulsive part of the Lennard-Jones is used. The energy scale is set by $\epsilon = \kappa_B T$ and the length scale by σ_b, both of which are set to unity in our simulations. Consistent with that, in this work all quantities are reported in reduced LJ units. The size of each bead in

real units should be considered as the thickness of DNA, i.e. $\sigma = 2.5$ nm or $= 2.5/0.34 \simeq 7.35$ bp per bead. The patches have no steric interactions.

Nearest-neighbour beads along the backbone are connected by finitely extensible nonlinear elastic (FENE) springs as

$$U_{\mathrm{FENE}}(r) = \begin{cases} -0.5kR_0^2 \ln\left(1-(r/R_0)^2\right) & r \leq R_0 \\ \infty & r > R_0 \end{cases} , \tag{2}$$

where $k = 40\epsilon/\sigma_b^2$ is the spring constant and $R_0 = 1.6\sigma_b$ is the maximum extension of the elastic FENE bond.

To model DNA's stiffness (150 bp or 50 nm) we introduce an additional bending energy penalty between consecutive triplets of neighbouring beads along the backbone in order to control polymer stiffness:

$$U_{\mathrm{bend}}(\theta_b) = k_\theta \left(1 + \cos\theta_b\right) . \tag{3}$$

Here, θ_b is the angle formed between adjacent bonds, i.e. $\boldsymbol{t}_i \cdot \boldsymbol{t}_{i+1}/|\boldsymbol{t}_i||\boldsymbol{t}_{i+1}|$ with $\boldsymbol{t}_i$ the tangent at i, and $k_\theta = 20\kappa_B T$ is the bending constant. With this choice $l_p = 20\sigma_b \simeq 50$ nm is the persistence length.

To model the torsional stiffness, two dihedral CHARMM springs constrain the relative rotation of consecutive beads, ψ, at a user-defined value (ψ_0). The torsional angle ψ is determined as the angle between planes defined by the triplets bead-bead-patch running along the DNA backbone. The potential is

$$U_{\mathrm{torsion}}(\psi) = k_\psi \left[1 + \cos\left(n\psi - d\right)\right] \tag{4}$$

where $k_\psi = 50k_BT$, $n = 1$ and $d = \psi_0$. The angle ψ_0 directly determines the thermodynamically preferred pitch of the twisted ribbon as $p = 2\pi/\psi_0$ and, in turn, this determines the preferred linking number as $Lk = M/p$, where M is the number of beads in the plasmid. In this model, we define the supercoiling as $\sigma \equiv Lk/M = 1/p$, which is set by initialising the

patchy-polymer as a flat ribbon and by subsequently imposing the angle ψ_0 in order to achieve the wanted σ (which may be zero, if $\psi_0 = 0$ or $p = \infty$).

Finally, to maintain consecutive beads parallel to the backbone, we constrain the angle between the triplets bead-bead-patch to $\pi/2$ so that the frames of reference formed by the triplets are aligned to each other. This potential is written as

$$U_{\text{align}} = k_a \left(1 + \cos\theta\right) \, . \tag{5}$$

where θ is the tilt angle as shown in Fig. 1 in the main text and with $k_a = 200 k_B T$.

The simulations are performed at fixed monomer density $\rho\sigma_b^3 = 0.08$ (equivalent to about 39 mg/ml of DNA), where $\sigma_b = 2.5$ nm$= 7.35bp$ is the typical size of a bead, and by evolving the equation of motion for the beads coupled to a heath bath which provides noise and friction. The equation of motion for each Cartesian component is thus given by

$$m_a \partial_{tt} r_a = -\nabla U_a - \gamma_a \partial_t r_a + \sqrt{2 k_B T \gamma_a}\eta_a(t) \, , \tag{6}$$

where m_a and γ_a are the mass and the friction coefficient of bead a, and η_a is its stochastic noise vector satisfying the fluctuation-dissipation theorem. U is the sum of the energy fields described above. The simulations are performed in LAMMPS (*36*) with $m = \gamma = k_B = T = 1$ and using a velocity-Verlet algorithm with integration time step $\Delta t = 0.002\,\tau_B$, where $\tau_B = \gamma\sigma^2/k_B T \simeq 0.03$ μs (using $\gamma = 3\pi\eta_{water}\sigma$ with $\eta_{water} = 1$ cP and $\sigma = 2.5$ nm) is the Brownian time. See also Table S1 for more details on the systems and Git repository `https://git.ecdf.ed.ac.uk/dmichiel/supercoiledplasmids/` for sample codes to reproduce these simulations.

Equilibration

Since we are simulating circular polymers (which are also torsionally constrained) we cannot use bridge algorithms to relax the chains, instead we typically perform equilibrium simulations

until key observables of the systems have reached a steady state. We monitor both, the gyration radius and the displacement of the molecules, and deem the system equilibrated when each molecule has travelled at least its own size in equilibrium. After that, we perform the production run.

In total, we have performed 20 sets of simulations, 5 supercoiling levels (relaxed, $\sigma = 0, 0.02, 0.04, 0.06$) per 4 choices of plasmid length ($M = 100, 200, 400, 800$). The number of plasmids in each system is $N = 160, 80, 40, 40$ meaning that there are 64'000 atoms per each system (and 128'000 for the one with $M = 800$, recall that each DNA bead is made by 4 atoms, one backbone and 3 patches). Thanks to the European Soft Matter Infrastructure we were able to run most of these simulations on the supercomputer JURECA and some on Vienna Scientific Cluster, consuming together about 2M CPU-h.

Intermediate Scattering Function - Simulations

In Fig. S5 we report the Intermediate scattering function (ISF) for monomers and centre of mass (COM) of the plasmids. We compute this as

$$ISF(q,t) = \langle e^{-i\boldsymbol{q}\cdot(\boldsymbol{r}_j(t)-\boldsymbol{r}_j(0))}\rangle_j \tag{7}$$

and averaged over monomers (or COMs) j. In particular, we use the convention that if $a = \boldsymbol{q}\cdot(\boldsymbol{r}_j(t)-\boldsymbol{r}_j(0)) < 0.1$ then $e^{-ia} = 1 - a^{2/6} + a^{4/120} - a^{6/5040}$ and $\sin(a)/a$ otherwise.

Detections of Tips and Plectonemes

The detection of tips and plectonomes in plasmids is done following the method described in Ref. (*64*). Briefly, we compute the absolute writhe of a segment s of a plasmid as

$$W(s) = \frac{1}{4\pi}\int_{s-l}^{s}\int_{s}^{s+l}\left|\frac{(\boldsymbol{r}_1-\boldsymbol{r}_2)\cdot(d\boldsymbol{r}_1\times d\boldsymbol{r}_2)}{|\boldsymbol{r}_1-\boldsymbol{r}_2|^3}\right| \tag{8}$$

where l is set to 50 beads as about 2 persistence lengths (which was shown to be a reasonable window size in Ref. (*64*)). This calculation yields a function $W(s)$ whose maxima represent regions of high local writhe and can identify tips of plectonemes. In addition to being a local maximum, we require that $W(s) > 0.35$ to avoid false positives. We checked that while the number of detected tips depends slightly on the threshold value and the tip length l, the primitive path analysis is robust with respect to usage of a more stringent choice of threshold 0.5 and $l = 40$. In Fig. S5 below we plot the average number of tips $\langle n_{\rm tips} \rangle$ per plasmid. One can readily notice that for low supercoiling the dispersion is quite large, indicating that the plasmids assume loose conformations with several tip-like segments along the contour. On the contrary, for large supercoiling one can notice that they become narrowly dispersed around $\langle n_{\rm tips} \rangle = 2$ indicating that the plasmids assume linear-like (rather than branched) conformations. Additionally, it is interesting to appreciate that $\langle n_{\rm tips} \rangle$ is very close to zero for short $M = 100$ plasmids with $\sigma = 0$ once again indicating locked swollen conformations, as shown in the main text.

Using the tip-detection algorithm we have also checked that there is no nematic order in our system as follows: for each chain we identify its two tips and construct the tip-to-tip vector $\boldsymbol{n}$. We then compute the nematic order parameter $S = \langle (3(\cos\theta)^2 - 1)/2 \rangle$ where θ is the angle between a reference $\boldsymbol{n}$ and that of the other chains in the system; the average is then performed over chains. We find values of $S \simeq 0.005 - 0.01$ for all systems for which tips can be identified unambiguously therefore indicating that there is no nematic order.

Primitive Path Analysis

The primitive path analysis for linear polymers (*66*) is based on fixing the chains' endpoints in space, switching off the intra-chain repulsive interaction, while keeping the inter-chain and running Langevin simulations at low temperature 0.01 to find a ground state. The resulting chain conformations (primitive paths) are composed of straight segments connected by sharp

kinks due to inter-chain entanglements. The entanglement length of each chain is then given by $M_e = \langle r_{\rm ee}^2 \rangle / ((M-1)\langle b_{pp} \rangle^2)$, where $\langle r_{\rm ee}^2 \rangle$ is the mean squared endpoint distance, $M-1$ is the number of bonds between the fixed points and $\langle b_{pp} \rangle$ is the mean bond-length of the primitive path averaged over a single chain. The final entanglement length is the average of M_e over many chains. We adapt the PPA for plasmids by fixing the tips of all detected plectonemes and then by following the same protocol as for linear chains.

For example, in the most common case of two tips per plasmid, both segments between the tips forming the plasmid contribute to M_e and are considered as independent for that purpose. In some cases the branch-detecting method fails to localize all tips and detects only one tip. In that case, we fix also the monomer $M/2$ contour-wise apart from a detected tip. In most cases this coincides with a tip detected with a lower detection threshold. If no tips are detected in one or more plasmids, the snapshot is excluded from the calculation. This does not happen for plasmids with $\sigma = 0.06$, happens rarely (in about 5% of cases) in for $\sigma = 0.04$ and frequently (about 60%) for the lower supercoiling $\sigma = 0.02$. This is natural as the less supercoiled plasmids display looser conformations where the branches are less clearly definable. We analyze about 50 to 100 snapshots each separated by at least $2.10^5 \tau_{\rm B}$. We check the method is robust with respect to the choice of the threshold value $0.35 - 0.5$ and the detection length $40 - 50$ beads, and gives within errorbars the same value of M_e. In contrast to equilibrium rings (*22*), we find our results do not strongly depend on the plasmid length, which gives the confidence that this method is reliable and highlights the role of linear-like entanglement present in systems of supercoiled plasmids. The small deviations within the errorbars are attributed to the finite size of the examined plasmids. For that reason we used only the longer systems with $M = 800$ and $M = 400$ to have at least $3 - 5$ statistically independent entanglement segments. Note that the value of M_e reported in the main text for the system $M = 400$ $\sigma = 0.02$ has no error bars because we analysed only one snapshot.

Isoconfigurational Averaging

To double-check our conclusions obtained using the primitive path analysis (PPA) we here consider the method of isoconfigurational averaging (*67*) as an alternative method to estimate the entanglement length. This method is based on running a set of NVE simulations with different initial velocities, but otherwise identical starting configuration. The resulting set of trajectories explore during sufficiently long averaging time t_{avg} the entanglement tube of the polymer, hence the mean over trajectories and over time t_{avg} defines the primitive path (PP), see Fig. S10. The Kuhn length of the PP, measured as full width at half-maximum of the tangent-tangent correlation function $C(s)$ defines the entanglement length. We slightly adapted the method, by using NVT ensemble with Langevin thermostat with different seed for each simulation, which allowed us to keep our original relatively high time step and not interfering with the method's idea. As the Langevin thermostat induces artificial random diffusion of the total center of mass, we subtracted it when analyzing the trajectories. The original method introduced in Ref. (*67*) was used on a system of rings linked through periodic boundary conditions, which allowed for the study of the PP without the complications arising from contour length fluctuations, constraint release or reptation. In our case, the method is affected by all of these and hence needs more testing to be used reliably in this context. Here we use it only as a tool to double check our findings from PPA and the growth of M_e with σ.

At first we tested the method on the system $M = 800$ and $\sigma = 0.04$, where the estimate of M_e from PPA is reasonably accurate (yielding $M_e \simeq 84$), but at the same time the plasmids exhibit non-trivial structure (some have more than two tips, some none). We ran 25 trajectories and used a range of different t_{avg}. We analysed each plasmid in the system separately and averaged over them to obtain $C(s)$. Short simulation or short averaging times would result in insufficient tube exploration, while long times would suffer from the changes in the primitive path due to the dynamic effects mentioned above, i.e. contour length fluctuations, constraint release

or reptation. Both of these problems tend to increase the measured M_e, but considering their different mechanism (tube exploration versus reptation, etc) we expect a different functional form dictating the enlargement of the tube size in the two regimes. Hence, to determine the appropriate averaging times we plotted M_e as function of runtime for different averaging times (Fig. S8). The estimations of M_e collapse for all averaging times suggesting that the ensemble of trajectories is large enough and there is no need for extensive time averaging. In log-log plot we observe, as expected, two distinct regimes of $M_e(t)$ and thus define the appropriate averaging time to be at the crossover of the two growth regimes, i.e. where tube exploration stops and reptation and other relaxation mechanisms start to be important. In this particular case, we find the crossover at about $10^4\tau_B$. The corresponding $M_e \simeq 54$. Although this does not numerically agree with the PPA method, as shown in (*67*), the values obtained from Isoconfigurational averaging tend to agree with other chain shrinking method that agrees with PPA up to a factor of about $3/2$ (*68*). Using this we find $M_e = 81$ in agreement with PPA. We repeated the analysis for system of linear chains (see next section) and systems with $M = 800$ and lower σ and as we show in the main text (Fig. 6F) the scaling of $M_e/M_{e,linear}$ appears to be the same as that found by PPA.

Further qualitative support for the time scale $10^4\tau_B$ is also evident from the snapshots of the alternative trajectories where we observe a significant ring fluctuations, particularly around the tips of the plasmid (Fig. S11).

Alternatively, one can quantify the tube radius r_T as the root mean square of the two lower eigenvalues of the gyration tensor of the alternative monomer positions see details in Ref. (*67*). We verified the results with this method only on $M = 800$ and $\sigma = 0.04$. Similarly to the previous one, yields an increasing function of the time, with a slightly less transparent regime boundary. Yet, if we use the same crossover time we get $r_T \simeq 23$ (Fig. S9). In linear melts the tube diameter is related to the entanglement length as $d_T = (l_K L_e)^{1/2}$, which, using effective

Kuhn length $l_K = 40$, for our values gives $M_e = L_e/\sigma_b = (2r_T)^2/l_K\sigma_b = 53$, consistent with the above value extracted using tangent-tangent correlation method on IsoMPs. Note that the tube diameter $2r_T$ is of the order of Kuhn length giving further confirmation that our system is in the crossover from semidilute to stiff regime as detailed in (*70*).

Let us stress that the entanglement effects and the proper definition of the entanglement length (or its equivalent) are not fully understood for ring polymers and even more so in case of supercoiled plasmids. For relaxed rings it has been shown (*81, 82*) that the "tube" inflates in a self-similar fashion. We highlight that the IsoMP method from Ref. (*67*) has the potential to elucidate this tube inflation for supercoiled plasmids versus linear DNA. We leave this for a future study.

Entanglement Length of Linear Twistable Chains

The PPA and IsoMP analysis was also performed on systems on linear twistable chains. They were prepared by removing a single bead from $M = 200$ beads long plasmids (with $\sigma = 0$) and re-equilibrating the system until the radius of gyration was in steady state (we also set the stiffness of the dihedral potential at 0). For PPA, we pinned the ends of the chains while for IsoMP we did the simulations as described in the previous section. We obtained $M_{e,linear} = 54$ with PPA and $M_{e,linear} = 49$ with IsoMP.

Supplementary Table

Supplementary Figures

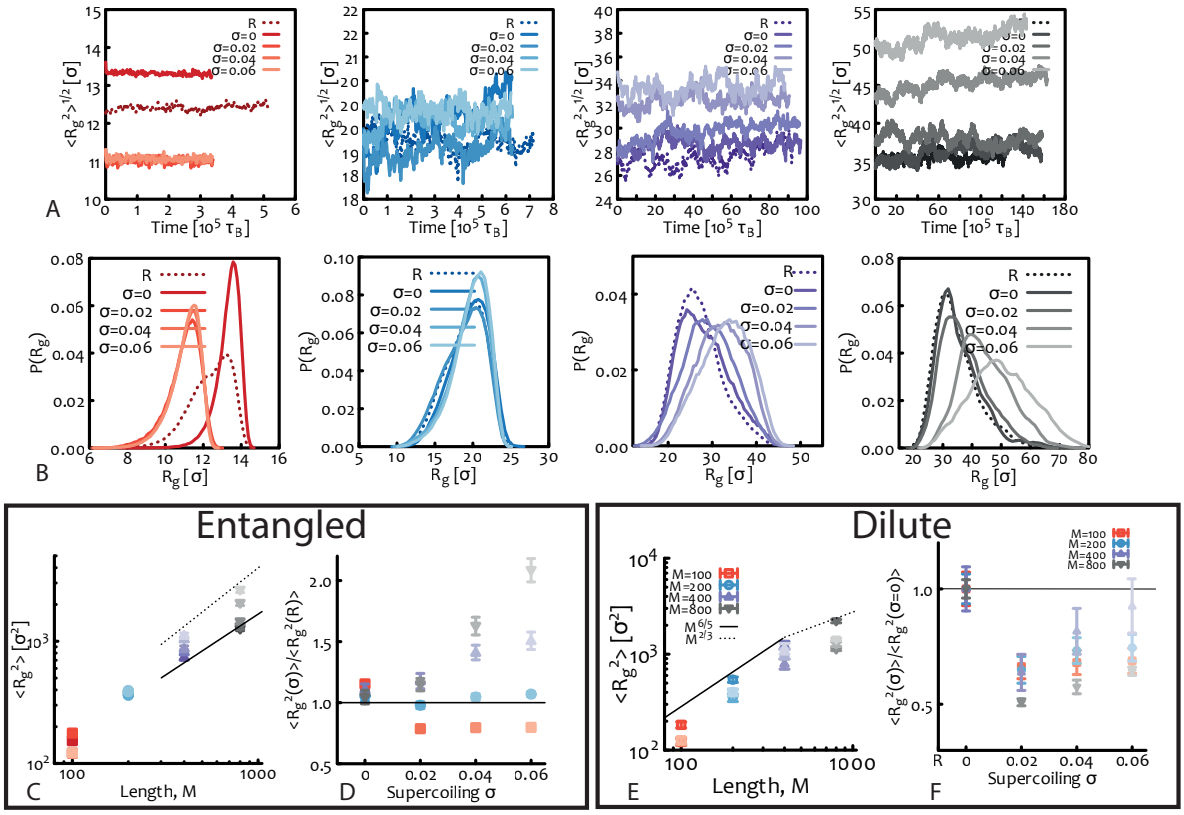

Figure S1: **A.** Time trace of the ensemble-averaged radius of gyration $\langle R_g^2 \rangle^{1/2}$ for $M = 100, 200, 400, 800$ (from left to right). **B.** Distributions of the radius of gyration. **C-D.** Scaling of the square radius of gyration as a function of length and supercoiling in **entangled** solutions. **E-F.** Scaling of the square radius of gyration as a function of length and supercoiling in **dilute** solutions, here we consider 10 times lower monomer density i.e. $\rho\sigma_b^3 = NM/L^3 = 0.008$.

M	N	σ	$\langle R_g^2\rangle/\sigma_b^2$	$\langle R_m^2\rangle/\sigma_b^2$	Σ/σ_b^2	$D.10^4\tau_B\sigma_b^2$	n_{tips}	$t_{total}/10^6\tau_B$	$t_{CPU}/10^4$hrs
100	160	R	154 (2)	357(10)	420 (125)	105 (1)	0.55 (0.58)	0.52	0.5
100	160	0	177 (1)	496 (7)	526 (83)	75 (4)	0.05 (0.08)	0.40	0.4
100	160	0.02	121 (1)	123 (3)	206 (28)	127 (5)	1.93 (0.12)	0.40	0.4
100	160	0.04	122 (1)	57 (2)	124 (12)	179 (5)	2.006 (0.007)	0.40	0.4
100	160	0.06	123 (1)	29 (1)	87 (8)	242 (2)	2.004 (0.005)	0.40	0.4
200	80	R	369 (9)	391 (20)	693 (244)	14 (2)	0.88 (0.62)	2.43	2.5
200	80	0	390 (16)	457 (31)	724 (238)	18 (2)	0.72 (0.53)	1.01	1
200	80	0.02	362 (10)	208 (10)	457 (70)	15 (2)	1.48 (0.52)	1.01	1
200	80	0.04	387 (10)	84 (4)	260 (24)	37 (2)	2.02 (0.05)	1.01	1
200	80	0.06	395 (8)	41 (2)	177 (12)	62 (2)	2.02 (0.02)	0.96	1
400	40	R	739 (37)	612 (35)	1385 (358)	1.8*	1.30 (0.91)	8.77	8.9
400	40	0	818 (34)	650 (37)	1398 (385)	1.6*	1.03 (0.75)	7.95	8.1
400	40	0.02	870 (46)	322 (19)	955 (146)	2.2*	1.59 (0.87)	7.91	8.0
400	40	0.04	1043 (45)	118 (8)	526 (44)	6.98 (0.01)	2.13 (0.32)	7.45	7.5
400	40	0.06	1114 (53)	53 (4)	349 (20)	15.80 (0.01)	2.04 (0.05)	7.28	7.3
800	40	R	1245 (32)	865 (55)	2623 (484)	0.4*	2.41 (1.57)	12.3	25
800	40	0	1262 (57)	807 (47)	2680 (495)	0.6*	1.94 (1.53)	15.8	32
800	40	0.02	1480 (61)	502 (31)	2042 (264)	0.5*	2.81 (1.77)	15.8	32
800	40	0.04	1966 (76)	167 (11)	1063 (79)	1.34 (0.01)	2.78 (1.00)	16.2	33
800	40	0.06	2524 (96)	67 (5)	684 (30)	2.89 (0.01)	2.16 (0.19)	13.9	28

Table S1: **System details**. Number in parenthesis correspond to the standard deviation. For the diffusion coefficient they represent the error on the fit on the last digit. Values of diffusion coefficient marked by * are upper estimates as the systems were not fully diffusive. Total simulation time 2M CPU-hours.

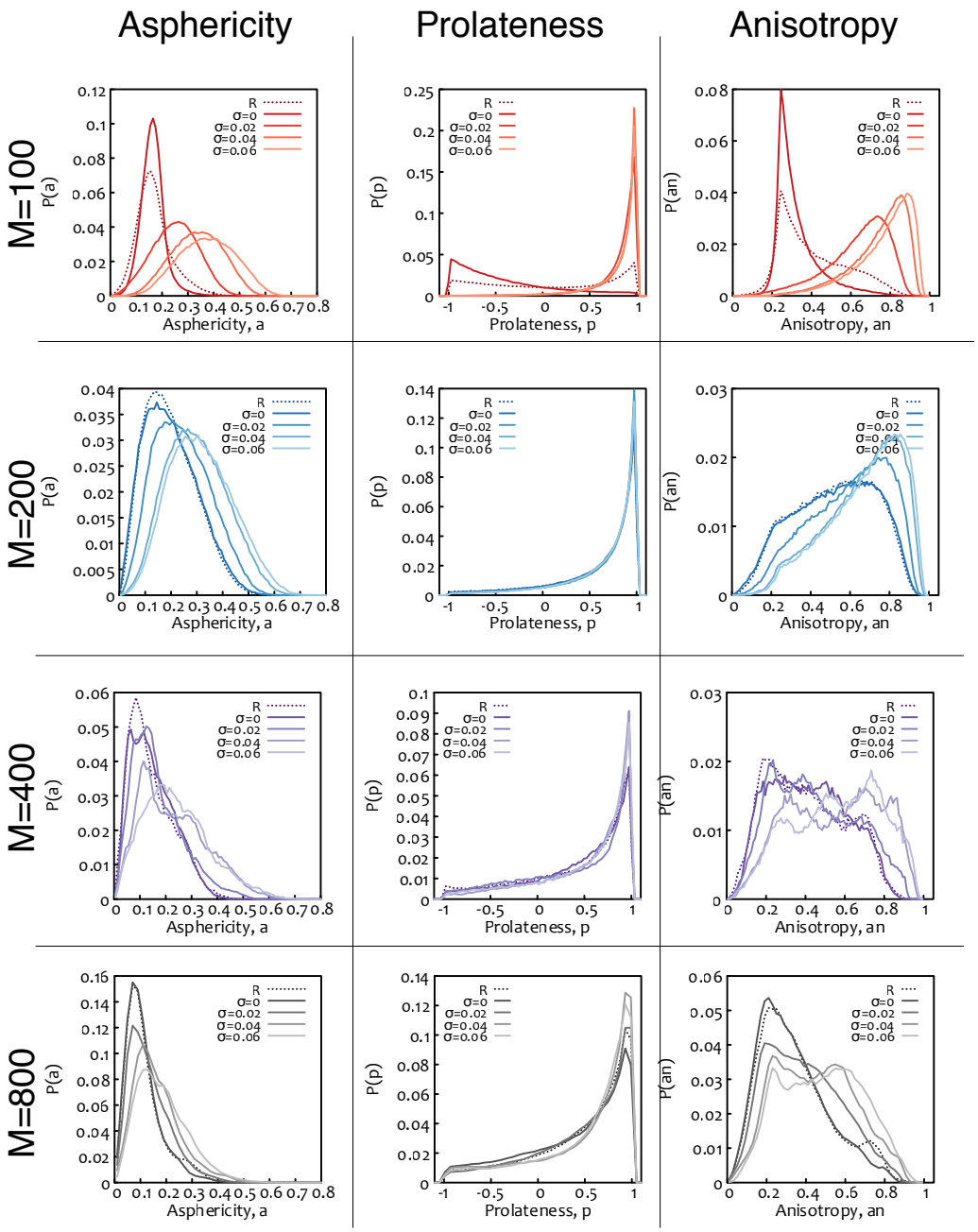

Figure S2: Asphericity (*50–52*) $a = ((a-b)^2 + (a-c)^2 + (b-c)^2)/2R_g^4$, prolateness $p = [(2a-b-c)(2b-a-c)(2c-a-b)] / \left[2(a^2+b^2+c^2-ab-ac-bc)^{3/2}\right]$ (*50*) and anisotropy $an = 3(a^2+b^2+c^2)/(2R_g^4) - 1/2$. a,b,c are the eigenvalues of the gyration tensor in descending order.

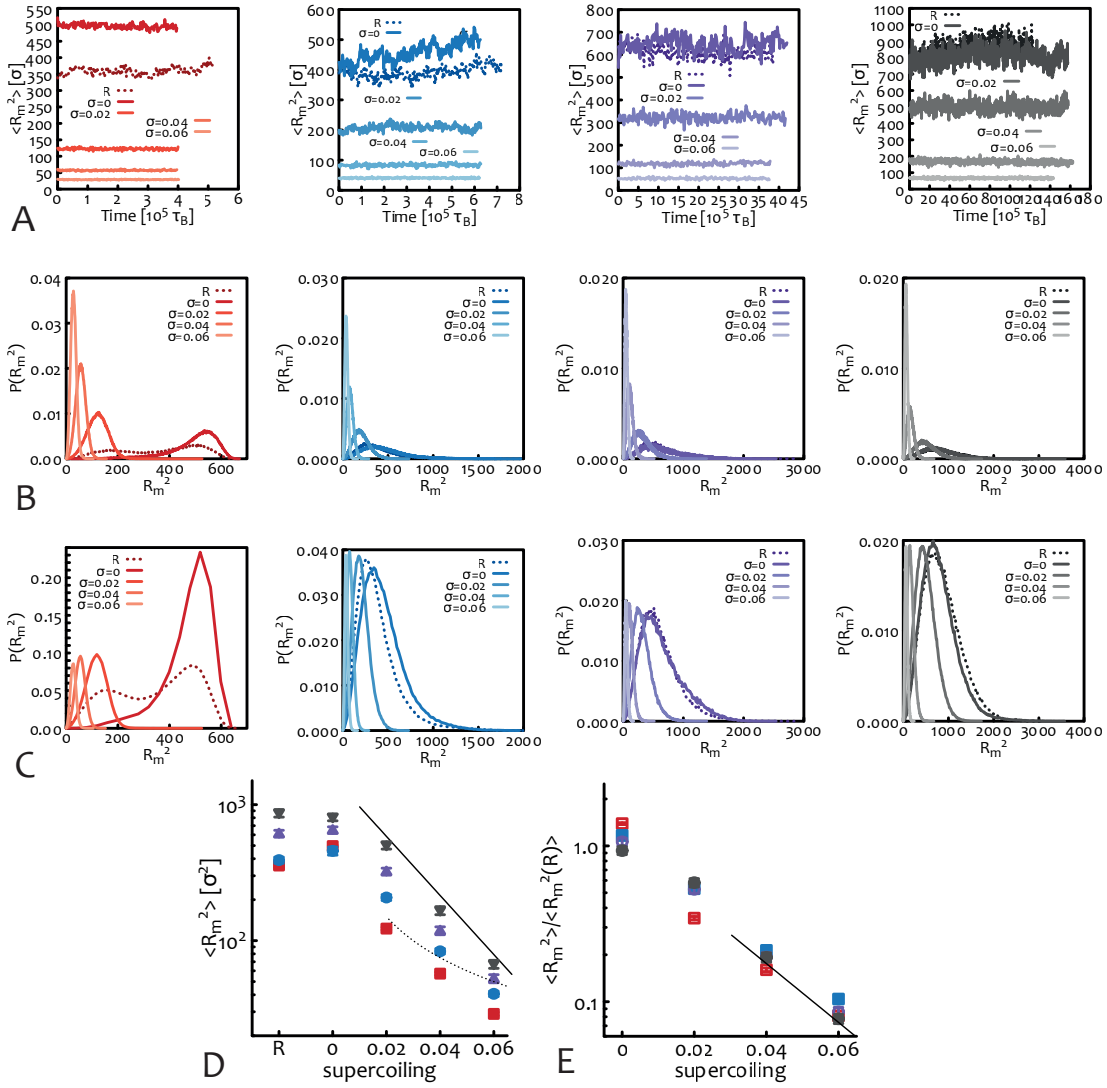

Figure S3: **A.** Time trace of the ensemble-averaged square magnetic radius $R_m^2 = |\boldsymbol{A}^2|/\pi$ with $\boldsymbol{A} = 1/2\sum_{i=1}^{N} \boldsymbol{r}_i \times \boldsymbol{r}_{i+1}$ (*58*). **B.** Distributions of the square magnetic radius for fixed bin width ($\Delta R_m^2 = 1$). **C.** Same as B, this time plotted for a fixed total number of bins (=1000) and different bin width to best compare the distributions (notice the bimodal distribution for relaxed plasmids $M = 100$). From left to right $M = 100, 200, 400, 800$. **D.** Scaling of the square magnetic radius with supercoiling. **E.** Same as D, normalised by the square magnetic radius of the relaxed plasmids. Solid lines show an exponential decay, whereas dashed line a power law $1/\sigma$. Notice that the scaling of R_m^2 with sigma is more compatible with an exponential decay than the power law. Instead the minimal surface (see main text) scales closely to $1/\sigma$.

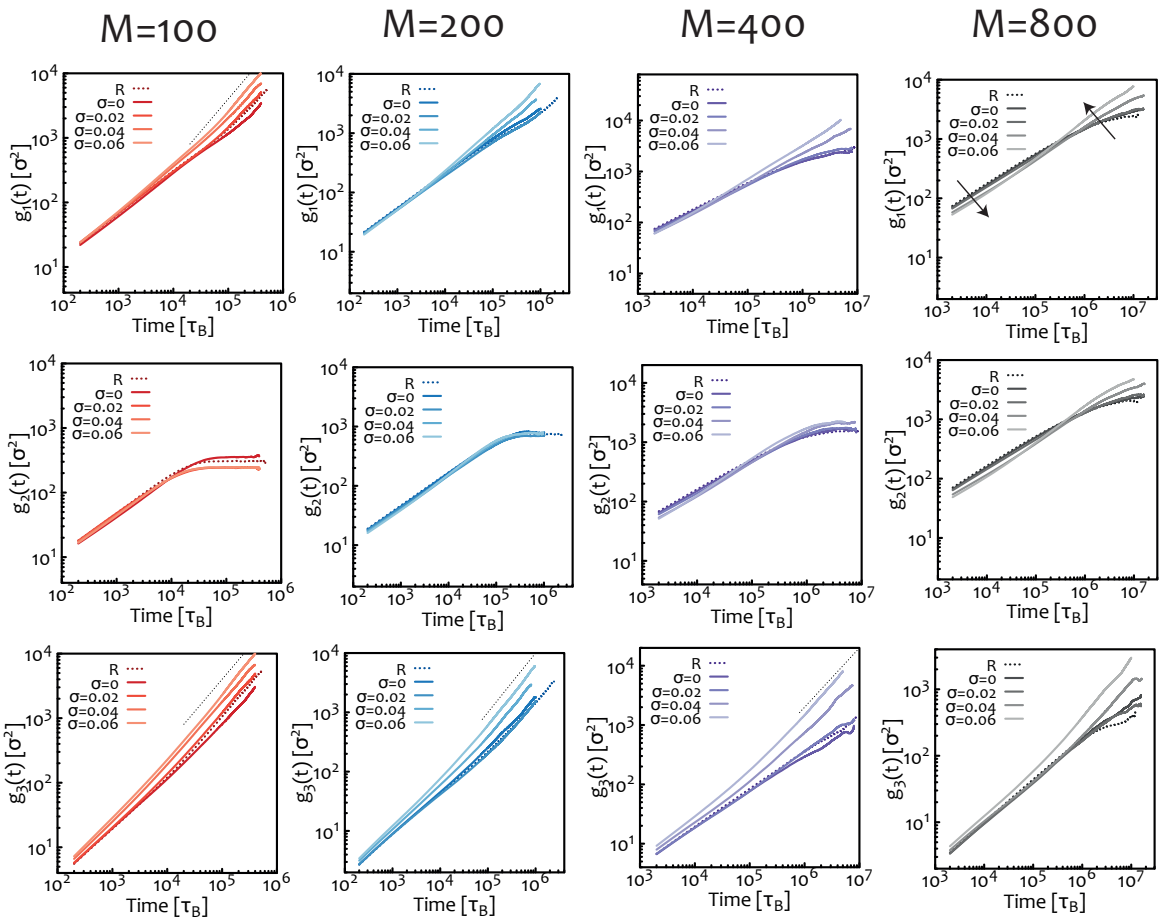

Figure S4: Plots of TAMSD, from top to bottom $g_1 = \langle[\boldsymbol{r}_i(t+t_0) - \boldsymbol{r}_i(t_0)]^2\rangle$, $g_2 = \langle[(\boldsymbol{r}_i(t+t_0) - \boldsymbol{r}_{cm}(t+t_0)) - (\boldsymbol{r}_i(t_0) - \boldsymbol{r}_{cm}(t_0))]^2\rangle$, $g_3 = \langle[\boldsymbol{r}_{cm}(t+t_0) - \boldsymbol{r}_{cm}(t_0)]^2\rangle$, where $\boldsymbol{r}_i(t)$ is the position of the monomer i at time t, $\boldsymbol{r}_{cm}(t)$ is the position of the centre of mass of the plasmid to which the monomer i belongs at time t and the averages are intended over monomers (and over plasmids) and times t_0. The arrows in the top right panel show that for $M = 800$, the monomer self-displacement is slower at short times and faster at larger times for increasing σ; this is in agreement with the more detailed ISF shown in Fig. S5.

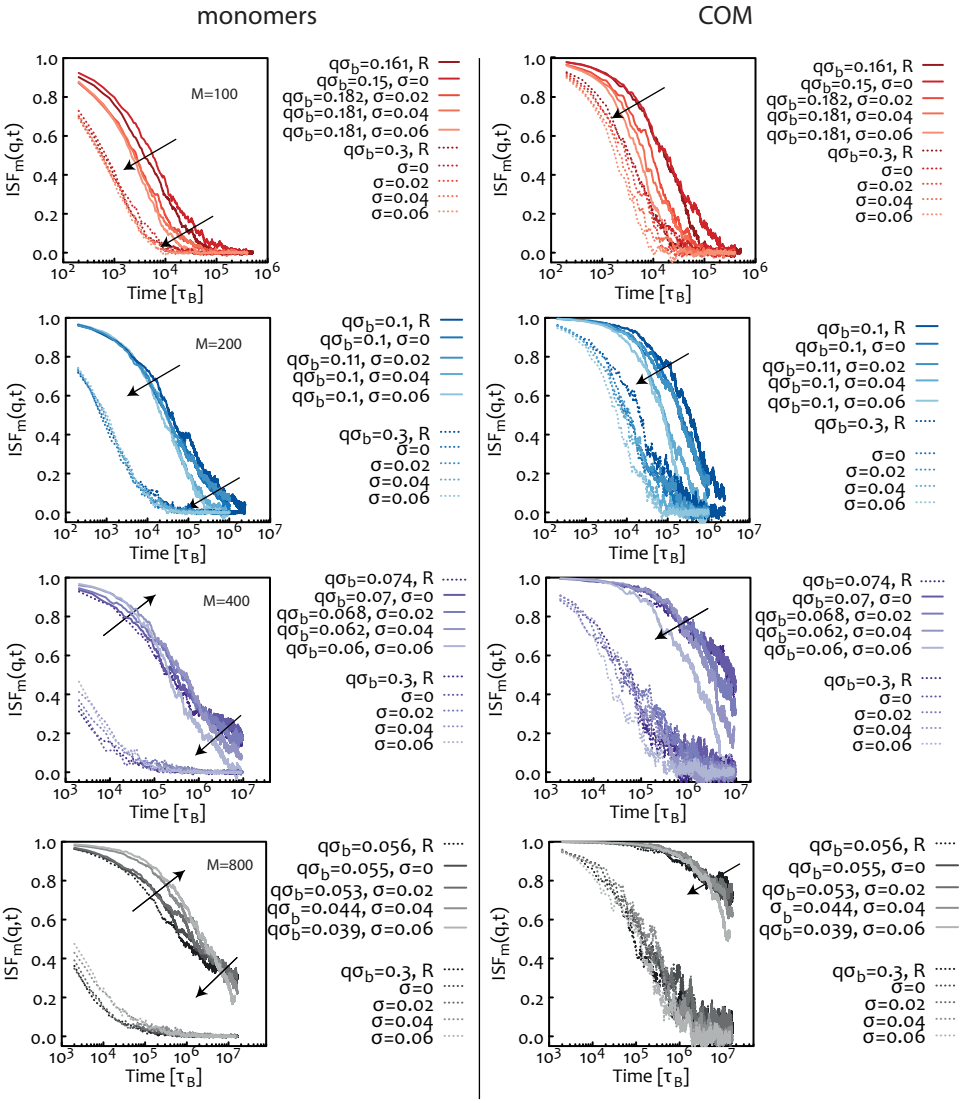

Figure S5: Plots of Intermediate scattering function for monomers (left) and centre of mass of plasmids (right). We chose to compare two values of q above and below the (inverse) plasmid size. In particular we picked $q_1 = 2/R_g$ corresponding to a length scale $l = 2\pi/q = \pi R_g$ above the diameter of the plasmids ($2R_g$, notice that $R_g = \langle R_g^2 \rangle^{1/2}$ depends on both length and value of supercoiling σ so it is slightly different for all the solid-line curves and we report the precise value in the legends) and $q_2 = 0.3\sigma^{-1}$ corresponding to a lengthscale comparable to the persistence length $l = 2\pi/q = 20\sigma$ (this is the same for all dashed-lines curves and so leave it unspecified). The arrows highlight the trend for increasing σ. In particular, for short chains both short and long timescales display faster decay of the monomer ISFs; on the other hand, for longer chains lengths ($M \geq 400$) one can see that systems with larger σ display a slower decay at short timescales and faster decay at longer timescales. This behaviour is similar at both wavelengths q but does not appear in the ISF of the COM. See also g_1 in Fig. S4.

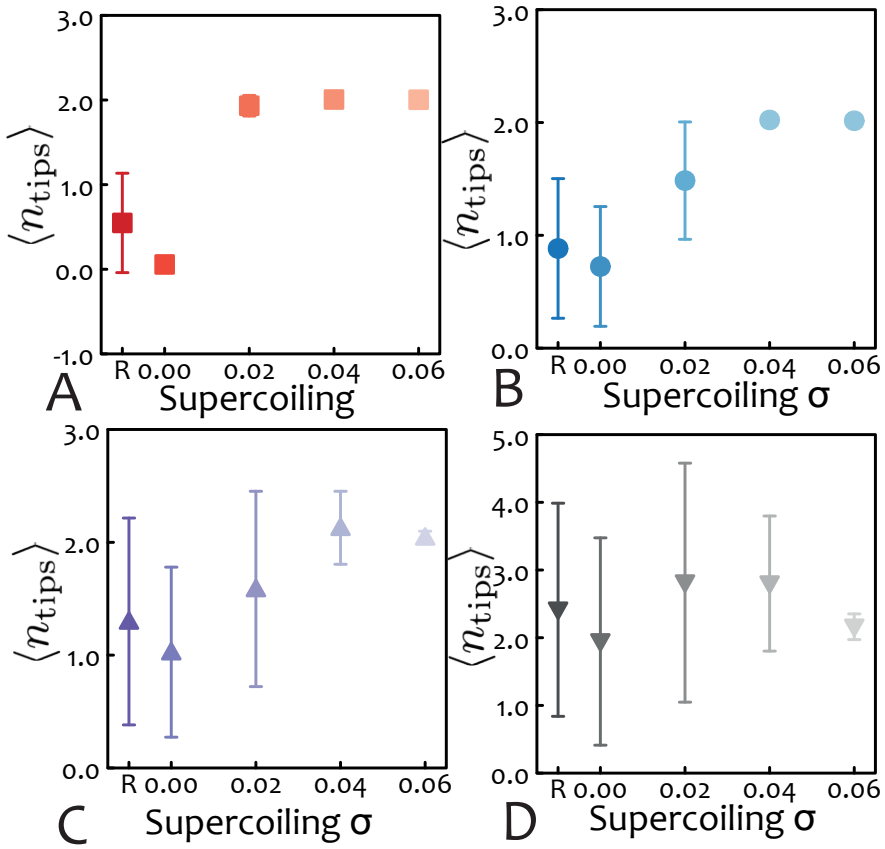

Figure S6: Plots of average number of tips for the different systems as a function of supercoiling. A. $M = 100$ B. $M = 200$ C. $M = 400$ D. $M = 800$.

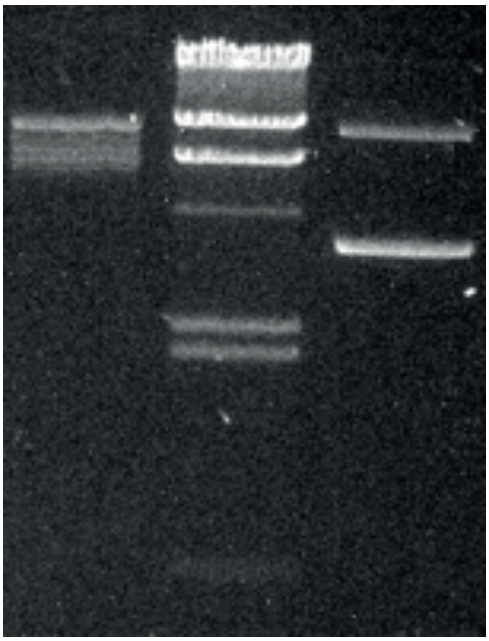

Figure S7: Analysis of DNA topology by agarose gel electrophoresis. From left to right: 5.9 kbp DNA after treatment with Topoisomerase I; λ-DNA HindIII digest used as a molecular weight standard (Thermo Fisher Scientific); 5.9 kbp DNA stock with no enzymatic treatment (80% supercoiled and 20% relaxed circular). Samples were run on a 1% agarose gel in 1X TAE buffer at 5 V/cm for 2.5 hours. Gel was post-stained (SYBR Safe DNA Gel Stain, Invitrogen).

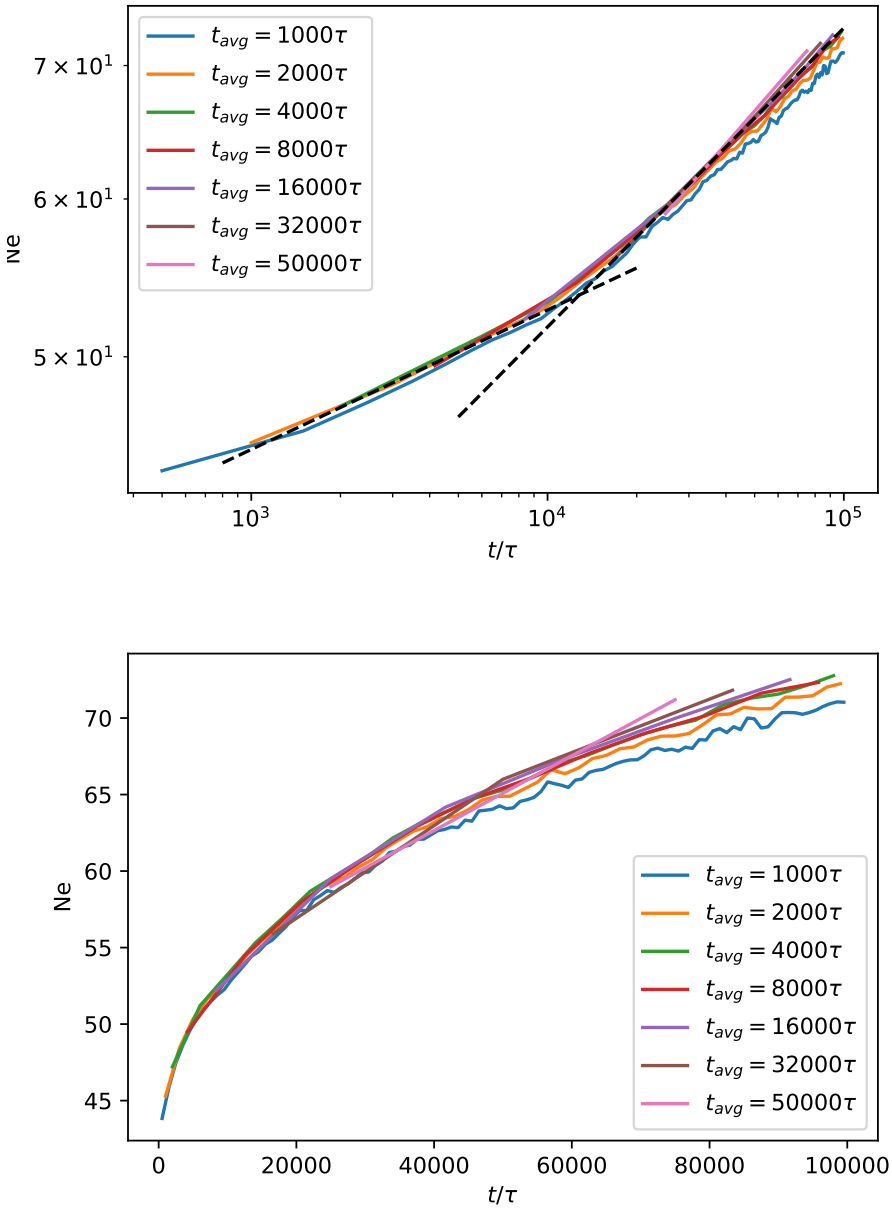

Figure S8: Entanglement length as function of time for different averaging times as extracted from the isoconfigurational averaging method. Top: log-log, two dashed lines (power-laws) serve as a guide to the eye and represent the two regimes: tube exploration and reptation/constraint release/etc (see text). Bottom: same as above but in linear-linear scale.

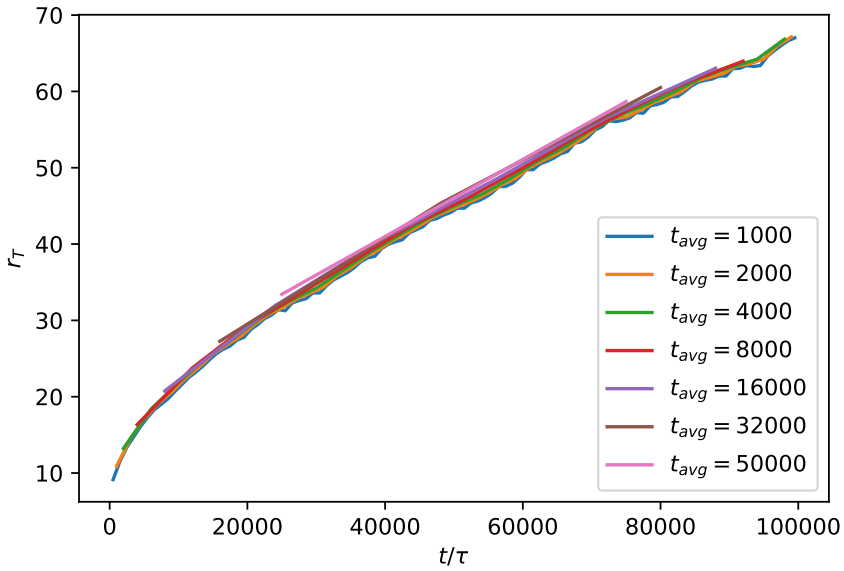

Figure S9: Tube radius versus time for different averaging times.

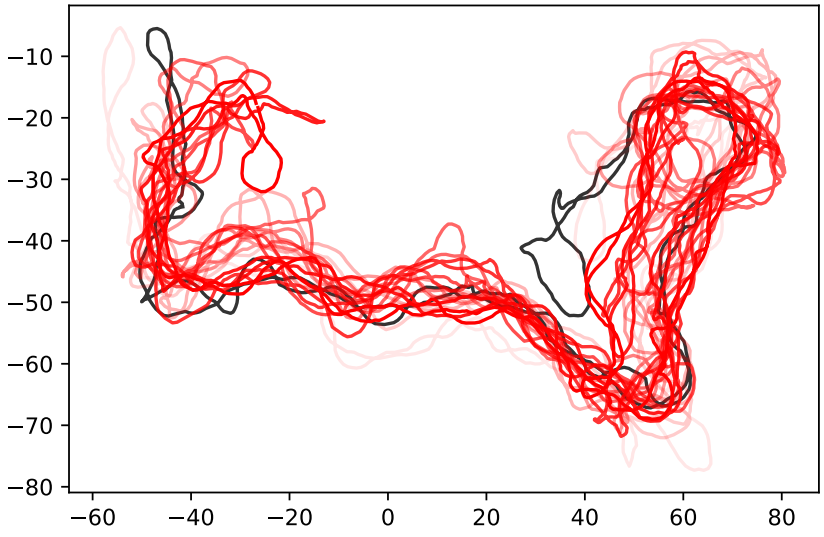

Figure S10: Ten snapshots of a conformation of a randomly chosen ring in time increments of $10^4\tau_B$. Decreasing opacity marks increasing time.

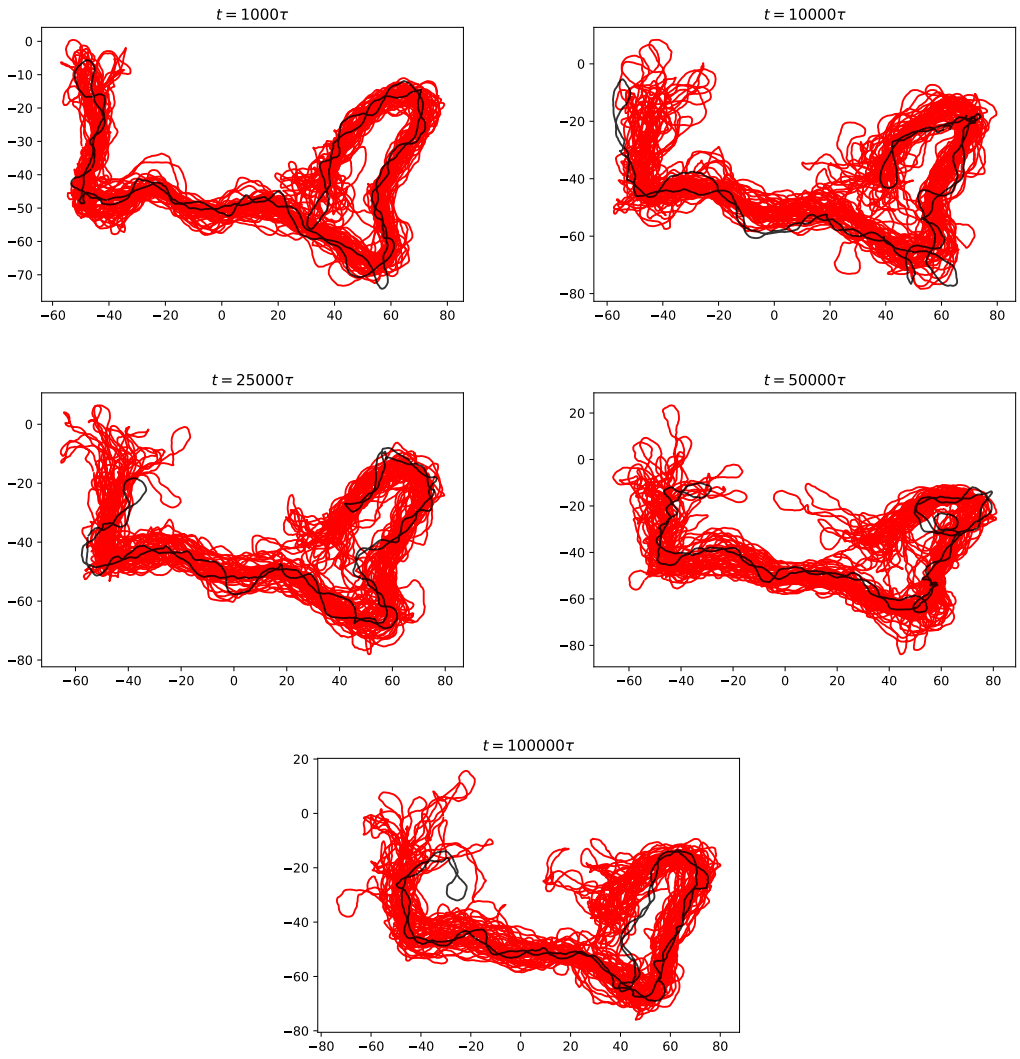

Figure S11: Snapshot of a randomly chosen ring (black) with its 24 alternative conformations (red) at a given simulation time in the title.